

Deoxygenation and Its Drivers Analyzed in Steady State for Perpetually Slower and Warmer Oceans



Key Points:

- Key drivers of deoxygenation are quantified for oxygen cycles idealized by being in equilibrium with perpetually slower oceans
- Widespread intense abyssal ocean deoxygenation is driven predominantly by slower circulations allowing respiration to act over longer times
- Most of the reduction in preformed oxygen is driven by changes in ventilation patterns and not by warming-driven reduced solubility

Correspondence to:

B. Pasquier and M. Holzer,
b.pasquier@unsw.edu.au;
mholzer@unsw.edu.au

Citation:

Pasquier, B., Holzer, M., Chamberlain, M. A., Matear, R. J., & Bindoff, N. L. (2024). Deoxygenation and its drivers analyzed in steady state for perpetually slower and warmer oceans. *Journal of Geophysical Research: Oceans*, 129, e2024JC021043. <https://doi.org/10.1029/2024JC021043>

Received 13 FEB 2024
 Accepted 15 AUG 2024

Author Contributions:

Conceptualization: Benoît Pasquier, Mark Holzer

Data curation: Benoît Pasquier, Mark Holzer

Formal analysis: Benoît Pasquier, Mark Holzer, Matthew A. Chamberlain, Richard J. Matear, Nathaniel L. Bindoff

Funding acquisition: Mark Holzer, Richard J. Matear, Nathaniel L. Bindoff

Investigation: Benoît Pasquier, Mark Holzer, Matthew A. Chamberlain

Methodology: Benoît Pasquier, Mark Holzer

Project administration: Mark Holzer

Resources: Mark Holzer

Software: Benoît Pasquier, Mark Holzer, Matthew A. Chamberlain

Supervision: Mark Holzer

Benoît Pasquier¹ , **Mark Holzer**¹ , **Matthew A. Chamberlain**² , **Richard J. Matear**² , and **Nathaniel L. Bindoff**³ 

¹School of Mathematics and Statistics, University of New South Wales, Sydney, NSW, Australia, ²Commonwealth Scientific and Industrial Research Organisation, Hobart, TAS, Australia, ³Australian Antarctic Program Partnership, Institute for Marine and Antarctic Studies, University of Tasmania, Hobart, TAS, Australia

Abstract Ocean deoxygenation is an important consequence of climate change that poses an imminent threat to marine life and global food security. However, our understanding of the complex interactions between changes in circulation, solubility, and respiration that drive global-scale deoxygenation is incomplete. Here, we consider idealized biogeochemical steady states in equilibrium with perpetually slower and warmer oceans constructed from climate-model simulations of the 2090s that we hold constant in time. In contrast to simulations of the end-of-century transient state, our idealized states are intensely deoxygenated in the abyss, consistent with perpetually reduced ventilation and throttled Antarctic Bottom Water formation. We disentangle the effects of the deoxygenation drivers on preformed oxygen and true oxygen utilization (TOU) using the novel concept of upstream exposure time, which precisely connects TOU to oxygen utilization rates and preformed oxygen to ventilation. For our idealized steady states, deoxygenation below 2,000 m depth is due to increased TOU, driven dominantly by slower circulations that allow respiration to act roughly 2–3 times longer thereby overwhelming the effects of reduced respiration rates. Above 500 m depth, decreased respiration and slower circulation closely compensate, resulting in little expansion of upper-ocean hypoxia. The bulk of preformed oxygen loss is driven by ventilation shifting equatorward to where warmer surface waters hold less oxygen. Warming-driven declines in solubility account for less than 10% of the total oxygen loss. Although idealized, our analysis suggests that long-term changes in the marine oxygen cycle could be driven dominantly by changes in circulation rather than by thermodynamics or biology.

Plain Language Summary Climate change is driving oxygen out of the ocean, threatening marine life and global food security. However, the precise contributions of the chemical, physical, and biological processes that control oxygen levels are not well known because of their complex interactions. To better understand these interactions, we consider idealized simulations of a global oxygen cycle that is fully equilibrated with a perpetually warmer and slower ocean constructed from climate-model simulations of the 2090s but held constant in time for our analyses. Compared to typical predictions, these idealized states exhibit intense deep-ocean deoxygenation, for which we precisely quantify the contributions from changes in solubility, respiration, and ocean circulation. We find that deep-ocean deoxygenation is driven by the slower circulation allowing respiration to act for 2–3 times longer thereby overcoming lower respiration rates. The surface origin of oxygen shifts away from cold high-latitude waters toward warmer waters, in which atmospheric oxygen is less soluble, further reducing oxygen levels. Warming-driven decreases in solubility alone only account for a mere 10% of the total oxygen loss. The upper ocean remains well oxygenated because changes in respiration and circulation compensate almost perfectly. Our results highlight the central importance of circulation in controlling oxygen in the ocean.

1. Introduction

The ocean has lost an estimated ~1–3% of its oxygen content over the last 50 years (e.g., Bindoff et al., 2022; Breiburg et al., 2018; Helm et al., 2011; Ito, 2022; Ito et al., 2017, 2024; Keeling & Garcia, 2002; Roach & Bindoff, 2023; Schmidtko et al., 2017; Whitney et al., 2007). Open-ocean deoxygenation is expected to continue in the future because of global warming, which reduces oxygen solubility and deep-ocean ventilation (e.g., Bopp et al., 2013; Keeling et al., 2010; Long et al., 2019; Matear & Hirst, 2003; Matear et al., 2000; Oschlies, 2021). There is broad consensus among models of the sixth Coupled Model Intercomparison Project (CMIP6) that

© 2024. The Author(s).

This is an open access article under the terms of the [Creative Commons Attribution-NonCommercial-NoDerivs License](https://creativecommons.org/licenses/by/4.0/), which permits use and distribution in any medium, provided the original work is properly cited, the use is non-commercial and no modifications or adaptations are made.

Validation: Benoît Pasquier, Mark Holzer, Matthew A. Chamberlain, Richard J. Matear, Nathaniel L. Bindoff
Visualization: Benoît Pasquier
Writing – original draft: Benoît Pasquier, Mark Holzer
Writing – review & editing: Benoît Pasquier, Mark Holzer, Matthew A. Chamberlain, Richard J. Matear, Nathaniel L. Bindoff

hypoxic zones will expand over the next century (e.g., in the Pacific; Busecke et al., 2022) to varying degrees depending on the future emissions' scenario (e.g., Kwiatkowski et al., 2020).

Ocean deoxygenation is increasingly recognized as posing an imminent threat to global marine ecosystems and food security (e.g., Earle et al., 2018; Laffoley & Baxter, 2019). Oxygen is essential for life (e.g., Falkowski & Godfrey, 2008). Long-term exposure to sufficiently low oxygen (severe hypoxia) can be lethal to marine organisms (e.g., Diaz & Rosenberg, 2008; Vaquer-Sunyer & Duarte, 2008). Mild to intermediate hypoxia has important physiological, behavioral, and ecological effects on marine ecosystems (e.g., Beman & Carolan, 2013; Ekau et al., 2010; McCormick & Levin, 2017; Morée et al., 2023; Pascal et al., 2023). Hence, the distribution of oxygen in the ocean is a key control on shaping marine habitats (e.g., Deutsch et al., 2015, 2024; Franco et al., 2022; Mongwe et al., 2024; Rogers, 2000; Sato et al., 2017; Seibel, 2011; Stramma et al., 2012). Even small O₂ declines and limited expansion of oxygen minimum zones (OMZs) are a major concern for global-ocean health (e.g., Deutsch et al., 2024; Gallo & Levin, 2016; Wishner et al., 2018).

Deoxygenation is driven by complex interactions among physical and biogeochemical processes that interact non-linearly on global scales. Oxygen in the ocean is controlled by air–sea exchange through surface winds and O₂ solubility, by photosynthetic production in the surface ocean, by bacterial respiration, and by the circulation which ventilates the ocean and connects these processes through the transport of dissolved oxygen to the deep ocean (e.g., Levin, 2018; Oschlies et al., 2018). To attribute O₂ changes quantitatively to specific driving mechanisms, a typical approach is to partition dissolved O₂ concentrations into a saturation concentration and apparent oxygen utilization (AOU; e.g., Bopp et al., 2002; Busecke et al., 2022; Couespel et al., 2019; Long et al., 2019; Schmidtko et al., 2017; Takano et al., 2023). To correct for AOU biases propagated by incomplete surface O₂ saturation (Ito et al., 2004), another common approach (using models) is to compute preformed oxygen and “true” oxygen utilization (TOU; e.g., Buchanan & Tagliabue, 2021; Cliff et al., 2021; Ito et al., 2022; Oschlies et al., 2019; Palter & Trossman, 2018). Studies based on these approaches agree qualitatively that increased oxygen utilization drives most of the deoxygenation, with reduced solubility accounting for less than 50% of upper-ocean deoxygenation, and less than ~25% of the deoxygenation of the entire water column. However, how much of the AOU (or TOU) increase can be attributed to changes in ventilation (i.e., circulation) versus respiration remains unclear (e.g., Breitburg et al., 2018; Oschlies et al., 2018).

While the importance of circulation for open-ocean hypoxia was recognized long ago (e.g., Sarmiento et al., 1988; Wyrski, 1962), its precise contribution to changes in preformed O₂ and oxygen utilization has yet to be quantified (Oschlies et al., 2018). This is a challenging task because disentangling the effects of circulation changes from the effects of changes in solubility and upstream respiration requires a careful accounting of all possible oxygen pathways and losses. To avoid these difficulties, some studies resort to perturbation experiments, under the tacit assumption that the system is sufficiently linear to infer the thermal and physical contributions to deoxygenation from the difference between perturbed and unperturbed simulations. These perturbed simulations may consist, for example, in keeping surface solubility fixed in time (e.g., Couespel et al., 2019; Matear & Hirst, 2003; Matear et al., 2000), in keeping oxygen utilization rates (OUR) fixed in time (e.g., Deutsch et al., 2006), in removing biogeochemical processes (e.g., Cliff et al., 2021), or in a combination of the above (e.g., Bopp et al., 2002; Plattner et al., 2001). To assess circulation control on oxygen loss, other perturbations consist in keeping the circulation fixed in its preindustrial state (e.g., Palter & Trossman, 2018). Such residual-based perturbation approaches can be strongly biased by spatial correlations between changes in solubility and changes in circulation that are typically ignored. However, as we show here, such correlations can be of first order for large perturbations or over long timescales. Also commonly used for assessing the effects of circulation changes on deoxygenation is the ideal mean age, often invoked as an empirical timescale linking TOU and OUR (e.g., Bopp et al., 2017; Busecke et al., 2022; Palter & Trossman, 2018). However, all the studies mentioned above ultimately fall short of accurately attributing deoxygenation to its drivers because they lack a quantitative framework, based on the underlying fundamental equations, that connects TOU to OUR with the correct circulation timescale.

Here, we address the following question: What would happen to oxygen if ocean biogeochemistry were allowed to equilibrate with a 2090s circulation that was frozen in time? To this end, we consider idealized steady oxygen cycles obtained by embedding the intermediate-complexity PCO₂ biogeochemistry model (Pasquier et al., 2023) into warmer and slower ocean states. These states are taken from climate-model simulations for the 2090s and then held fixed (or “frozen”) in time for perpetuity. The equilibrated steady-state oxygen cycle is obtained using a Newton solver and compared to preindustrial conditions. Equilibrated steady states allow us to probe the oxygen

cycle on all the fundamental timescales of the associated ocean transport (e.g., fast thermocline vs. slow abyssal ventilation). In particular, our approach captures the very longest timescales that cannot be probed with typical centennial-scale transient simulations. In addition, steady states afford many computational advantages that we exploit extensively. Note, however, that this framework does not capture natural variability on any timescale (e.g., seasonal, interannual).

We rigorously partition O_2 changes into contributions from circulation changes, solubility changes, and their spatial correlations by employing the exact timescale that connects TOU to upstream OUR. Specifically, in steady state, the local OUR contribution at location r to the TOU content of an interior volume Ω has recently been shown to be $OUR(r) \times \Gamma_{\Omega}^{\uparrow}(r)$, where $\Gamma_{\Omega}^{\uparrow}(r)$ is the “upstream exposure time,” that is, the time that the water in Ω spent sweeping past upstream location r , and hence the time over which $OUR(r)$ acts (Holzer, 2022). Importantly, $\Gamma_{\Omega}^{\uparrow}$ is a fundamental timescale of the circulation only. Furthermore, we show here that $\Gamma_{\Omega}^{\uparrow}$ also connects the preformed O_2 content of Ω to its surface origin.

Our idealized biogeochemical steady states exhibit intense abyssal deoxygenation because of perpetually reduced ventilation and throttled Antarctic Bottom Water (AABW) formation (Holzer et al., 2020), which stands in stark contrast to typical transient simulations of the late 21st century. While our idealized states cannot capture realistic transient evolution, they nevertheless inform us on the long-timescale mechanisms that drive deoxygenation. We find that the intense abyssal deoxygenation in our idealized steady states is characterized by widespread expansion of mild to severe hypoxia. Above 500 m depth, hypoxic regions do not expand appreciably because decreases in preformed oxygen are compensated by colocated TOU reductions, driven primarily by reduced respiration rates. Below 2,000 m depth, by contrast, strong increases in TOU are predominantly driven by the slower perpetual 2090s circulation allowing respiration to act 2 to 3 times longer. Preformed oxygen declines almost everywhere, driven primarily by equatorward shifts in ventilation caused by reduced AABW and North Atlantic Deep Water (NADW) formation, with reduced solubility only playing a secondary role (order 10% of the total oxygen loss). Our analyses highlight the overarching importance of the circulation in determining the ocean's oxygen content through its control on ventilation patterns and the path-integrated oxygen utilization.

2. Methods

2.1. Frozen-In-Time Preindustrial and 2090s Ocean Circulations

We consider three idealized ocean states that are frozen in time: a preindustrial state that is used as the reference and two perpetually warmer and slower ocean states. Specifically, we use decadal averages of simulations from the Australian Community Climate and Earth System Simulator (ACCESS1.3; Bi et al., 2013; Marsland et al., 2013). Decadal mean circulation and thermodynamic state variables (including temperature and salinity) are then held constant in time for perpetuity. The 1990s decadal average is used as an approximation for the preindustrial state, and 2090s decadal averages corresponding to an intermediate and a worst-case climate-change scenario (Representative Concentration Pathways RCP4.5 and RCP8.5; Meinshausen et al., 2011, 2020) are used to represent the perpetually warmer and slower ocean states. For further details, see the work of Pasquier et al. (2024), who used the same framework of steady-state biogeochemistry embedded in frozen-in-time circulations to quantify carbon-cycle changes.

We emphasize that we do not assume that our perpetual-2090s circulations corresponds to a steady state of the ocean dynamics. Instead, we simply freeze the mean 2090s ocean state in time and analyze the idealized steady-state oxygen cycle that is in equilibrium with this perpetually slower and warmer ocean. Our results thus cannot be interpreted as predictions of the future. However, despite our idealized framework requiring a number of caveats (Section 4.1), our results inform us on the key mechanisms that drive deoxygenation in the real ocean. Working with steady states has several advantages, the most important of which is that it allows us to capture the biogeochemical response on the longest timescales of the circulation. In addition, steadiness has the practical advantages of obviating the need for time stepping and avoiding the complications of transience. In particular, steadiness made it possible to precisely decompose and separate the drivers of deoxygenation.

The advective–diffusive flux–divergence operator of each state is organized into a sparse transport matrix following Chamberlain et al. (2019). The horizontal advective fluxes were directly averaged from the ACCESS1.3 output while the vertical advective fluxes were inferred from mass conservation by integrating the horizontal divergence upward from the seafloor. Horizontal and vertical diffusion is included in the transport matrix with background

diffusivities of $500 \text{ m}^2 \text{ s}^{-1}$ (horizontal) and $10^{-5} \text{ m}^2 \text{ s}^{-1}$ (vertical), and a mixed-layer vertical diffusivity of $0.1 \text{ m}^2 \text{ s}^{-1}$. To construct the transport matrix, we used the decadal mean of the yearly maximum mixed-layer depth as simulated by ACCESS1.3. The model grid employed (coarse-grained from the original ACCESS1.3 grid) has a nominal horizontal resolution of $2^\circ \times 2^\circ$ (finer in the tropics) and 50 vertical levels with thicknesses increasing from 10 m at the surface to 335 m at depth. We used the same horizontal and vertical diffusivities for the preindustrial and 2090s states, and all our calculations account for both advection and diffusion.

When interpreting our results it is important to note that like most state-of-the-art climate models, the ACCESS1.3 circulation features an unrealistically deep mixed layer in the Southern Ocean compared to observations (Bi et al., 2013; de Boyer Montégut et al., 2004; de Lavergne et al., 2014). For the ACCESS1.3 simulations we used, the mixed layers reach below 5,000 m near the Weddell and Ross Seas in the 1990s and strongly shoal in the 2090s, which imprints on our results. Although abyssal ventilation and bottom-water formation through convection are unrealistic (e.g., Heuzé et al., 2013), the key realistic model behavior for our purposes here is a decline in Southern Ocean deep ventilation driven by climate change: Antarctic Bottom Water formation has been observed to decline in recent decades and is predicted to decline strongly over the next few decades (e.g., Chen et al., 2023; de Lavergne et al., 2014; Gunn et al., 2023; Li et al., 2023) (Detailed caveats of the circulation model are discussed in Section 4.1).

2.2. Oxygen Model

We use the PCO2 biogeochemistry model of Pasquier et al. (2023). PCO2 is embedded in the frozen-in-time ocean circulations using our transport matrices, and we solve directly for the biogeochemical steady state using a Newton solver. Our steady-state oxygen cycles thus correspond to the equilibrium that would ultimately be reached if the 2090s thermodynamic and physical state of the ocean were held fixed in time for perpetuity.

A key feature of PCO2 for capturing the response of dissolved oxygen to a change in ocean state is that PCO2 explicitly models the nonlinear interactions and feedbacks between oxygen, carbon, and nutrients. This includes the effects of oxygen and particulate organic matter on respiration, and the effects of temperature on biological production and respiration. The biogeochemical parameters of PCO2 were objectively optimized for preindustrial conditions against observations of phosphate, dissolved inorganic carbon, total alkalinity, and oxygen (The same parameter values were then used for all our states). The optimized O_2 field has a global volume-weighted root-mean-square model–observations mismatch of $\sim 30 \mu\text{M}$ (Pasquier et al., 2023). Systematic biases, in part inherited from the parent ACCESS-model circulation, remain despite parameter optimization, with underestimated O_2 in the upper tropical Pacific and Atlantic above $\sim 1,000 \text{ m}$ and overestimated O_2 in the Southern Ocean and in the tropical Indian Ocean (see Figure A1 for a comparison between modeled and observed zonal mean $p\text{O}_2$). We deem these biases acceptable as they are smaller than for most CMIP5 models (Bao & Li, 2016) and because they are generally dwarfed by the much larger changes analyzed here.

In the PCO2 model, oxygen enters and exits the ocean through air–sea gas exchange, is photosynthetically produced in the euphotic layer, and utilized through aerobic bacterial respiration. In steady state, the three-dimensional O_2 concentrations obeys

$$\mathcal{T} \text{O}_2 = P - \text{OUR} + J_{\text{atm}}, \quad (1)$$

where the frozen-in-time transport operator \mathcal{T} acts on O_2 concentrations such that $\mathcal{T} \text{O}_2 = \nabla \cdot (\mathbf{u} \text{O}_2) - \nabla \cdot \mathbf{K} \nabla \text{O}_2$ is the divergence of the advective–diffusive flux of O_2 due to velocity \mathbf{u} and eddy diffusion (diffusivity tensor \mathbf{K}). $P = r_{\text{O}_2:\text{C}} U_{\text{C}}$ is the photosynthetic production of oxygen keyed to biological carbon uptake U_{C} through the optimized $r_{\text{O}_2:\text{C}} = 1.31 \text{ molO}_2 \text{ molC}^{-1}$, and $\text{OUR} = r_{\text{O}_2:\text{C}} (R_{\text{DOC}} + R_{\text{POC}}) \Theta(\text{O}_2 - \text{O}_2^{\text{lim}})$ is the oxygen utilization rate keyed to respiration of dissolved and particulate organic carbon (R_{DOC} and R_{POC}) (The Θ term switches off aerobic respiration when O_2 drops below $\text{O}_2^{\text{lim}} = 5 \mu\text{M}$, implicitly representing the effect of anaerobic denitrification). Air–sea gas exchange is modeled using the parameterization $J_{\text{atm}} = k(K_0 p\text{O}_2^{\text{atm}} - \text{O}_2)/h$ at the surface (Wanninkhof, 2014), where k is the wind- and temperature-dependent gas-transfer velocity, K_0 is the temperature- and salinity-dependent oxygen solubility, $p\text{O}_2^{\text{atm}}$ is the oxygen atmospheric partial pressure (based on an atmospheric oxygen mixing ratio of 0.210 for both preindustrial and perpetual-2090s states), and $h = 10 \text{ m}$ is the thickness of the top model layer (see Section 4.1 for discussion on the caveats of the biogeochemistry model).

We organize the grid values of concentrations into column vectors and discretized linear operators into corresponding sparse matrices. The nonlinear system of biogeochemical tracer equations is solved for steady state using a Newton solver. In matrix form, the vector of oxygen concentrations, \mathbf{O}_2 , is the solution to $\mathbf{T}\mathbf{O}_2 = \mathbf{P} - \mathbf{OUR} + \mathbf{J}_{\text{atm}}$, where \mathbf{T} is the discretized advective–diffusive flux–divergence operator (“transport matrix” for short) such that $\mathbf{T}\mathbf{O}_2$ is the vector of the divergence of the advective–diffusive flux of oxygen, and \mathbf{P} , \mathbf{OUR} , and \mathbf{J}_{atm} are the vectors of photosynthetic oxygen production, oxygen utilization, and air–sea oxygen exchange, respectively.

2.3. Preformed Oxygen, $\mathbf{O}_2^{\text{pre}}$

Preformed oxygen is defined here as the oxygen that would be propagated by the ocean circulation out of the euphotic-layer and into the ocean's interior in the absence of any aphotic sources and sinks. We use the base of the euphotic zone rather than the base of the mixed layer to define preformed oxygen for convenience and consistency with the definitions of preformed and regenerated phosphate and carbon in the related work of Pasquier et al. (2023, 2024). Hence, $\mathbf{O}_2^{\text{pre}}$ depends only on euphotic \mathbf{O}_2 concentrations and on ventilation patterns.

In matrix form, the vector of preformed oxygen concentrations, $\mathbf{O}_2^{\text{pre}}$, is conveniently computed by solving $(\mathbf{T} + \mathbf{L})\mathbf{O}_2^{\text{pre}} = \mathbf{L}\mathbf{O}_2$, where \mathbf{L} is a diagonal matrix with diagonal values of 1 s^{-1} in the euphotic zone and 0 otherwise, enforcing $\mathbf{O}_2^{\text{pre}} = \mathbf{O}_2$ in the euphotic zone (only the euphotic-zone values of \mathbf{O}_2 are used in $\mathbf{L}\mathbf{O}_2$). (For such short relaxation time, there is no sensitivity to its precise value; 10 s gives indistinguishable results).

To separate the effects of solubility from the effects of circulation on \mathbf{O}_2 within the euphotic zone, we further decompose $\mathbf{O}_2^{\text{pre}}$ into a saturated component $\mathbf{O}_2^{\text{sat}}$ and a disequilibrium component $\mathbf{O}_2^{\text{dis}} = \mathbf{O}_2^{\text{pre}} - \mathbf{O}_2^{\text{sat}}$. This decomposition is useful because the air–sea \mathbf{O}_2 disequilibrium varies with location and can be important in deep-water formation regions (see, e.g., Duteil et al., 2013; Eggleston & Galbraith, 2018; Ito et al., 2004; Russell & Dickson, 2003).

2.4. True Oxygen Utilization, TOU

To quantify the oxygen deficit caused by respiration, we use “true oxygen utilization” $\text{TOU} = \mathbf{O}_2^{\text{pre}} - \mathbf{O}_2$ (e.g., Broecker & Peng, 1982; Holzer, 2022; Ito et al., 2004; Koeve & Kähler, 2016). TOU is thus the cumulated amount of oxygen that has been removed by respiration along its interior transit since leaving the euphotic zone. The vector of TOU grid values is computed similarly to $\mathbf{O}_2^{\text{pre}}$ by solving $(\mathbf{T} + \mathbf{L})\text{TOU} = \mathbf{OUR}$ (Holzer, 2022). Note that $-\text{TOU}$ may also be thought of as regenerated oxygen, $\mathbf{O}_2 - \mathbf{O}_2^{\text{pre}}$ (e.g., DeVries & Deutsch, 2014).

2.5. Deoxygenation Drivers

To summarize the contributions to deoxygenation from changes in circulation, solubility, or respiration, it is useful to integrate the oxygen change over a specific volume Ω of interest. We will first consider TOU and then $\mathbf{O}_2^{\text{pre}}$.

2.5.1. Change in TOU

The Ω inventory of TOU is controlled at every location \mathbf{r} upstream of Ω by $\text{OUR}(\mathbf{r})$ and by the time that the water currently in Ω spent flowing past \mathbf{r} , which is the time for which $\text{OUR}(\mathbf{r})$ acts on the oxygen heading toward Ω . This timescale, which we call “upstream exposure time” here, was only recently derived and computed by Holzer (2022), who showed that for steady flow it is equal to $\Gamma_{\Omega}^{\dagger}(\mathbf{r})$, the mean time that water currently at \mathbf{r} will spend in Ω on its way to the surface (Figure 1). In steady state, $\Gamma_{\Omega}^{\dagger}(\mathbf{r})$ equals the time that oxygen at \mathbf{r} was exposed to respiration upstream of Ω and connects the TOU inventory to $\text{OUR}(\mathbf{r})$ through the relationship (Holzer, 2022):

$$\int_{\Omega} \text{TOU}(\mathbf{r}) d^3\mathbf{r} = \int \text{OUR}(\mathbf{r}) \Gamma_{\Omega}^{\dagger}(\mathbf{r}) d^3\mathbf{r}. \quad (2)$$

We emphasize that the upstream exposure time ($\Gamma_{\Omega}^{\dagger}$ in steady state) is fundamentally different from the ideal mean age (e.g., Primeau, 2005), which is commonly used to approximately relate TOU or AOU to OUR (e.g., Bopp et al., 2017; Doney & Bullister, 1992; Feely et al., 2004; Palter & Trossman, 2018; Warner et al., 1996; Zheng

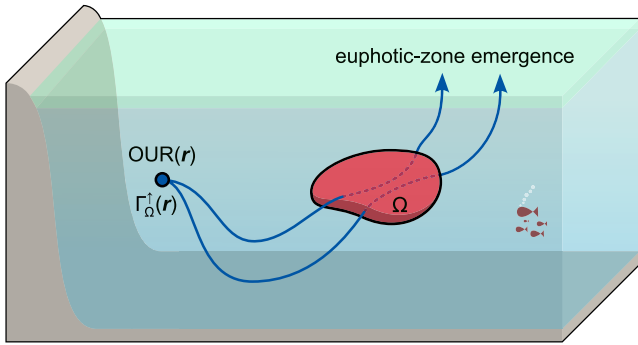


Figure 1. The upstream exposure time at any interior location r (blue dot) is the time that water currently in interior volume Ω (red region) spent at r in the past (integrated over all paths and past times; blue lines). It is thus the total time for which the water in Ω was exposed to oxygen utilization at upstream location r in the past. This allows us to connect the oxygen “missing” in Ω (the Ω -integrated TOU) to the oxygen utilization rate (OUR) at r . In steady state, this upstream exposure time equals $\Gamma_{\Omega}^{\uparrow}(r)$, the mean time that water currently at location r will spend in Ω on its way to the euphotic zone (see also Equation 2 and Holzer, 2022).

et al., 1997, to cite a few), despite known systematic biases (e.g., Brandt et al., 2015; Duteil et al., 2013; Koeve & Kähler, 2016; Sonnerup et al., 2013, 2015; Thomas et al., 2020).

The integrals in Equation 2 are easily computed in matrix form. That is, Equation 2 can be written as $\Omega^T \mathbf{V} \mathbf{T} \mathbf{O} \mathbf{U} = \mathbf{O} \mathbf{U}^T \mathbf{V} \Gamma_{\Omega}^{\uparrow}$, where \mathbf{V} is a diagonal matrix with the grid-box volumes along the diagonal, Ω is a mask vector with entries of 1 for grid cells in Ω and entries of 0 otherwise, and the \uparrow superscript denotes the matrix transpose. The upstream exposure time obeys $(\tilde{\mathbf{T}} + \mathbf{L}) \Gamma_{\Omega}^{\uparrow} = \Omega$ (Holzer, 2022), where $\tilde{\mathbf{T}} = \mathbf{V}^{-1} \mathbf{T}^T \mathbf{V}$ is the volume-weighted adjoint of \mathbf{T} , which governs the time-reversed adjoint flow.

The connection of TOU with OUR through $\Gamma_{\Omega}^{\uparrow}$ in Equation 2 allows us to partition TOU changes into contributions from changes in respiration, circulation, and their interaction. Specifically, we algebraically decompose, at every point r of the ocean, the change in the integrand $(\text{OUR} \times \Gamma_{\Omega}^{\uparrow})$ on the right-hand-side of Equation 2 as

$$\Delta(\text{OUR} \times \Gamma_{\Omega}^{\uparrow}) = \underbrace{\Gamma_{\Omega}^{\uparrow} \Delta \text{OUR}}_{\text{respiration}} + \underbrace{\text{OUR} \Delta \Gamma_{\Omega}^{\uparrow}}_{\text{circulation}} + \underbrace{\Delta \text{OUR} \Delta \Gamma_{\Omega}^{\uparrow}}_{\text{cross term}}, \quad (3)$$

where a quantity X not preceded by Δ denotes its preindustrial value and ΔX denotes the change in X for the state embedded in the perpetual-2090s circulations. The driving process represented by each term is indicated beneath the braces of Equation 3, and these terms are globally integrated to give the corresponding contributions to the changes in the Ω inventory of TOU in accord with Equation 2. The $\Gamma_{\Omega}^{\uparrow} \Delta \text{OUR}$ term corresponds to the contribution from respiration-only changes, with the circulation fixed at its preindustrial state, while $\text{OUR} \Delta \Gamma_{\Omega}^{\uparrow}$ corresponds to the contribution from circulation-only changes, with OUR fixed at its preindustrial value, and the “cross term” $\Delta \text{OUR} \Delta \Gamma_{\Omega}^{\uparrow}$ corresponds to the colocated changes in OUR and $\Gamma_{\Omega}^{\uparrow}$. To the best of our knowledge, this is the first decomposition to cleanly separate respiration-only and circulation-only effects, and to explicitly account for the effect of concurrent changes in both respiration and circulation.

2.5.2. Change in O_2^{pre}

In steady state, the Ω inventory of preformed oxygen is determined by euphotic oxygen concentrations modulated by the amount of Ω -volume ventilated per unit area at the base of the euphotic zone, $\mathcal{V}_{\Omega}^{\downarrow}$. Mathematically,

$$\int_{\Omega} \text{O}_2^{\text{pre}}(r) d^3 r = \int \text{O}_2(r_s) \mathcal{V}_{\Omega}^{\downarrow}(r_s) d^2 r_s, \quad (4)$$

where location r_s ranges over the base of the euphotic layer. The matrix form of Equation 4 is $\Omega^T \mathbf{V} \mathbf{O}_2^{\text{pre}} = \mathbf{O}_2^T \mathbf{A} \mathcal{V}_{\Omega}^{\downarrow}$ where \mathbf{A} is a diagonal matrix with the horizontal area of each grid cell along the diagonal and where $\mathcal{V}_{\Omega}^{\downarrow} = \mathbf{A}^{-1} \mathbf{L} \mathbf{V} \Gamma_{\Omega}^{\uparrow}$. One can derive these relationships by noting that just like **OUR** is the source term for **TOU**, the equation for preformed oxygen shows that $\mathbf{L} \mathbf{O}_2$ is the effective source term for O_2^{pre} . By replacing **OUR** with $\mathbf{L} \mathbf{O}_2$ and **TOU** with O_2^{pre} in the matrix form of Equation 2, we obtain $\Omega^T \mathbf{V} \mathbf{O}_2^{\text{pre}} = \mathbf{O}_2^T \mathbf{L} \mathbf{V} \Gamma_{\Omega}^{\uparrow}$. This relationship provides a direct connection between the O_2^{pre} inventory of Ω and the flux of $\Gamma_{\Omega}^{\uparrow}$ into the euphotic zone, because $\Gamma_{\Omega}^{\uparrow}$ traces the O_2^{pre} in Ω back to its euphotic origin (We note in passing that this link stems from the equivalence between concentration propagated forward in time from a boundary condition and the flux into that boundary from a unit-injected mass propagated in the time-reversed adjoint flow (e.g., Holzer & Hall, 2000)).

The Ω volume ventilated per unit area $\mathcal{V}_{\Omega}^{\downarrow}$ is a generalization of the ocean volume ventilated per unit area (e.g., Holzer et al., 2020; Primeau, 2005). $\mathcal{V}_{\Omega}^{\downarrow}$ provides a quantitative connection between the Ω inventory of O_2^{pre} and euphotic O_2 concentrations. We note in passing that $\mathcal{V}_{\Omega}^{\downarrow}$ is proportional to the volume fractions f_{ij} derived by Fu

et al. (2018) for quantifying OMZ ventilation, through $f_{ij} = A_{ij} \mathcal{V}_{\Omega}^{\downarrow} / v_{\Omega}$, where A_{ij} is the surface grid cell area and v_{Ω} is the Ω volume.

Similar to our analysis of TOU changes, we partition changes in the Ω inventory of O_2^{pre} into contributions from changes in solubility and circulation. To this end, we algebraically decompose, at every point r_s at the base of the euphotic layer, the change in the integrand $O_2 \mathcal{V}_{\Omega}^{\downarrow}$ on the right-hand-side of Equation 4 as

$$\Delta(O_2 \mathcal{V}_{\Omega}^{\downarrow}) = \underbrace{\mathcal{V}_{\Omega}^{\downarrow} \Delta O_2^{\text{sat}}}_{\text{solubility}} + \underbrace{O_2^{\text{sat}} \Delta \mathcal{V}_{\Omega}^{\downarrow} + \Delta(O_2^{\text{dis}} \mathcal{V}_{\Omega}^{\downarrow})}_{\text{circulation}} + \underbrace{\Delta O_2^{\text{sat}} \Delta \mathcal{V}_{\Omega}^{\downarrow}}_{\text{cross term}}, \quad (5)$$

where we have further separated euphotic O_2 into its saturated and disequilibrium components, and the corresponding driving processes are indicated with braces. The term $\mathcal{V}_{\Omega}^{\downarrow} \Delta O_2^{\text{sat}}$ accounts for the contribution to ΔO_2^{pre} in Ω from solubility-only changes, keeping the circulation (and thus ventilation volumes $\mathcal{V}_{\Omega}^{\downarrow}$) fixed in its preindustrial state. The contribution from circulation-only changes includes $O_2^{\text{sat}} \Delta \mathcal{V}_{\Omega}^{\downarrow}$, where solubility in the euphotic zone is fixed at its preindustrial values, and $\Delta(O_2^{\text{dis}} \mathcal{V}_{\Omega}^{\downarrow})$, which we consider to be a circulation-only effect by assuming that O_2^{dis} is entirely driven by circulation changes. The decomposition of Equation 5 is, to the best of our knowledge, also new.

2.6. Hypoxia Severity Categories

To quantify the extent of low-oxygen conditions, we follow Hofmann et al. (2011) and define hypoxia categories A, B, and C, ranging from mild to severe in terms of the in situ effective partial pressure of oxygen, pO_2 . Specifically for our model, category-A mild hypoxia is deemed to occur where $pO_2 \leq 100$ matm, category-B intermediate hypoxia where $pO_2 \leq 50$ matm, and category-C severe hypoxia where $pO_2 \leq 15$ matm. Note that we have adjusted the $pO_2 = 106, 60,$ and 22 matm thresholds of Hofmann et al. (2011) such that the modeled global hypoxia volume for each category matches the values based on GLODAPv2 observations (Lauvset et al., 2016). Despite matching the global hypoxic volumes, the horizontal extent of hypoxic regions remain overestimated in the Pacific and Atlantic and underestimated in the Indian Ocean (see Figures A2 and A3 for more details).

3. Results

3.1. Global Deoxygenation and Expansion of Hypoxic Regions

We find intense deoxygenation for our steady-state oxygen cycles embedded in the perpetual-2090s ocean states, with the global oxygen inventory decreasing by 30% and 60% for the RCP4.5- and RCP8.5-based states, respectively. Figure 2 shows the basin zonal-mean pO_2 for each scenario and the corresponding change from preindustrial to perpetual-2090s states (We show the effective partial pressure, pO_2 , because it is the most relevant thermodynamic oxygen quantity for critical physiological processes in living organisms (Hofmann et al., 2011)). The oxygen loss is largest in the Pacific because of the dramatically reduced ventilation from AABW. Oxygen loss is also intense in the Atlantic sector of the Southern Ocean, but deoxygenation in the Atlantic is overall less pronounced as the mid-depth North Atlantic remains ventilated by North Atlantic Deep Water (NADW) in the perpetual-2090s circulations. Deoxygenation does not occur everywhere however, with slight increases in the zonal mean pO_2 occurring close to the surface in each basin, particularly at northern mid-latitudes in the Atlantic and Indian Ocean (Figures 2j–2o), likely due to reduced local respiration and shoaling NADW.

The expansion of hypoxic zones depends strongly on the severity (i.e., pO_2 threshold) of hypoxia considered, on the local ventilation, and on the climate-change scenario. Figure 3 shows the profiles of the spatial extent of each hypoxia category (Section 2.6), over each basin, and for each scenario. The expansion of hypoxic regions is larger for RCP8.5 than for the less extreme RCP4.5 scenario. We find that low-oxygen conditions generally expand toward the seafloor in the deep ocean rather than toward the surface. In the Pacific, expansion is maximal with all abyssal waters becoming moderately hypoxic (cat. B; $pO_2 \leq 50$ matm) for RCP4.5 and severely hypoxic (cat. C; $pO_2 \leq 15$ matm) for RCP8.5. Similarly, all Indian Ocean waters below roughly 800 m become mildly hypoxic for RCP4.5 and moderately hypoxic for RCP8.5. In the Atlantic, the volume of severe hypoxia changes little, while mild and intermediate hypoxia only strongly expand for RCP8.5 at intermediate and abyssal depths. In the

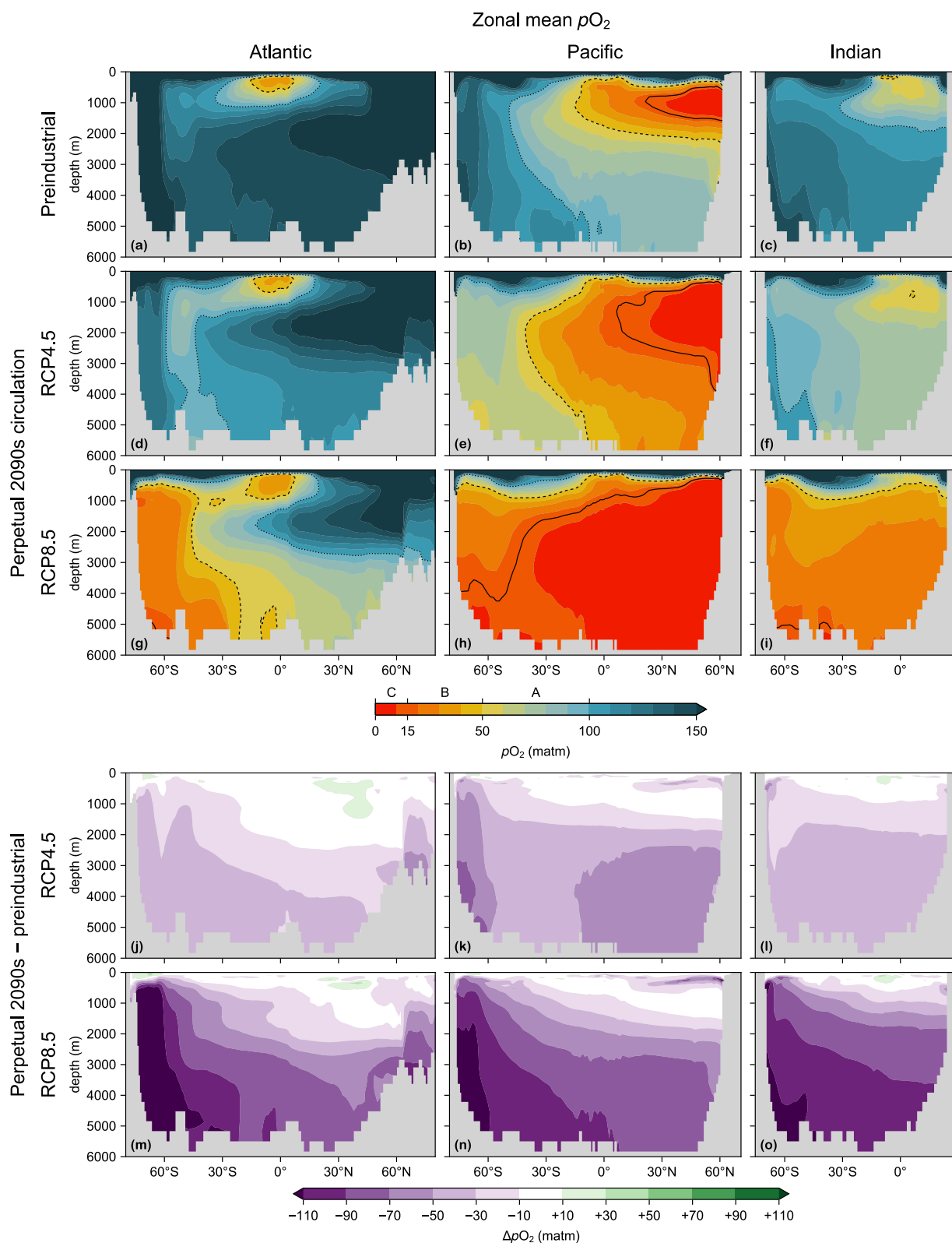


Figure 2. (a) Atlantic, (b) Pacific, and (c) Indian Ocean zonal-mean pO_2 for the preindustrial state. The dotted, dashed, and solid contour lines indicate the $pO_2 = 100$, 50, and 15 matm thresholds of hypoxia categories A, B, and C, respectively. (d–f) As (a–c) for the state with perpetual-2090s circulation of the RCP4.5 scenario. (g–i) As (d–f) for RCP8.5. (j–o) As (d–i) for the change from the preindustrial state to the perpetual-2090s states. The Atlantic basin excludes the Gulf of Mexico and the Caribbean, and the Pacific basin excludes the Sea of Japan so that the zonal means are more cleanly interpretable.

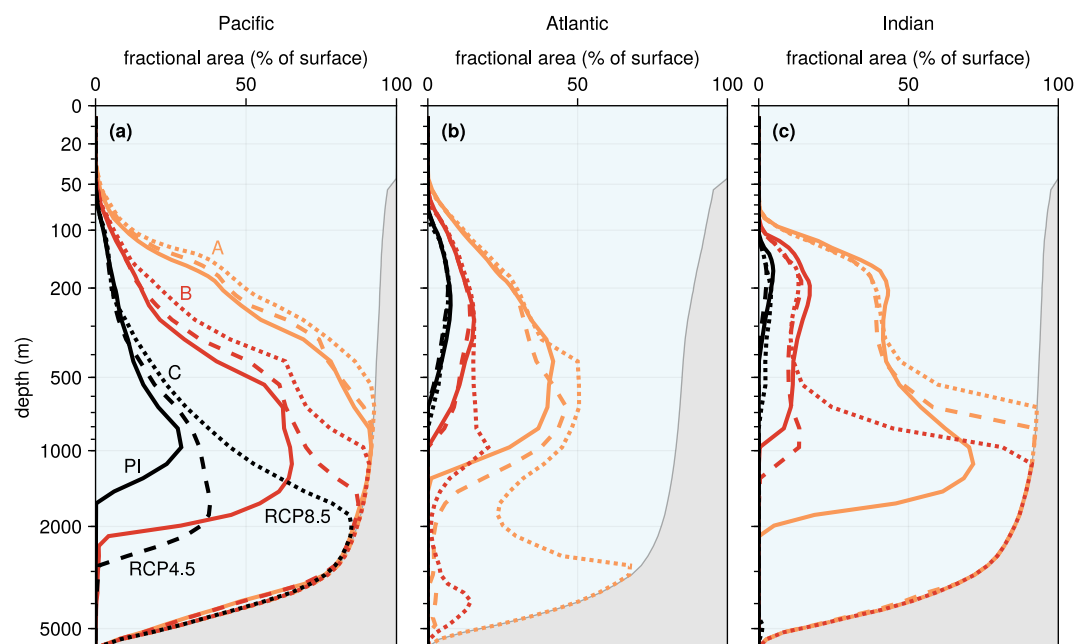


Figure 3. (a) Pacific depth profiles of the spatial extent of mild (A, orange; $pO_2 \leq 100$ matm), intermediate (B, red; $pO_2 \leq 50$ matm), and severe hypoxia (C, black; $pO_2 \leq 15$ matm) for the preindustrial state (PI; solid lines), the perpetual RCP4.5 2090s state (dashed lines), and the perpetual RCP8.5 2090s state (dotted lines). The spatial extent for a given hypoxia category and depth is quantified by the ratio of the horizontal hypoxic area to the surface area of the corresponding ocean basin (The gray area represents the seafloor). (b) As (a) for the Atlantic. (c) As (a) for the Indian Ocean. Note the nonlinear depth scale.

Atlantic and Indian Ocean above 500 m, the areal extent of hypoxia actually contracts slightly as pO_2 has slight increases there (cf. Figures 2j–2o discussed above).

To visualize the horizontal distribution of expanding hypoxic conditions, we consider the vertical water-column minimum pO_2 shown in Figure 4. In the preindustrial state, oxygen minimum zones are located in the eastern tropical sectors of the major basins and in the North Pacific. In the perpetual-2090s states, global-scale expansion of low-oxygen conditions is visible for RCP4.5, except in the North Atlantic and in the Atlantic sector of the Southern Ocean, which remain ventilated ($pO_2 \geq 100$ matm) by NADW and AABW. Intermediate hypoxia expands southward beyond southern mid-latitudes, while severe hypoxia expands into the tropics. For the RCP8.5-based state, mild hypoxia occurs across the entire global ocean (although predominantly at depth as shown in Figure 3), while intermediate hypoxia occurs across the entire Pacific, South Atlantic, and Indian Ocean, and severe hypoxia extends across the entire Pacific only, reaching as far as the Southern Ocean.

3.2. Drivers of Deoxygenation

3.2.1. Changes in TOU and Preformed Oxygen

Deoxygenation occurs through declines in preformed oxygen and through increases in true oxygen utilization (TOU; see Section 2), which may also be thought of as negative regenerated oxygen (i.e., $O_2^{reg} = -TOU$; see, e.g., DeVries & Deutsch, 2014). Qualitatively, reduced respiration drives TOU decreases while a slower circulation drives TOU increases by allowing more time for respiration to act. Thus, TOU can either increase or decrease (Figure B1) depending on which effect dominates. We find that in the upper ocean TOU decreases because of reduced OUR and in the deep ocean TOU increases because of longer circulation timescales (upstream exposure times; Figure B2). Preformed oxygen, by contrast, declines over most of the ocean (Figure B1), in part because of warming-driven solubility decreases and importantly, as we will show below, because of an equatorward shift in ventilation. With warmer future sea surface temperature (SST), surface O_2 concentrations decrease almost everywhere, except in the North Atlantic “cold blob” (e.g., Cheng et al., 2022) where temperatures decrease, and near the Weddell and Ross Seas where the mixed layer shoals (Figure B3). Shoaling of the ACCESS model's

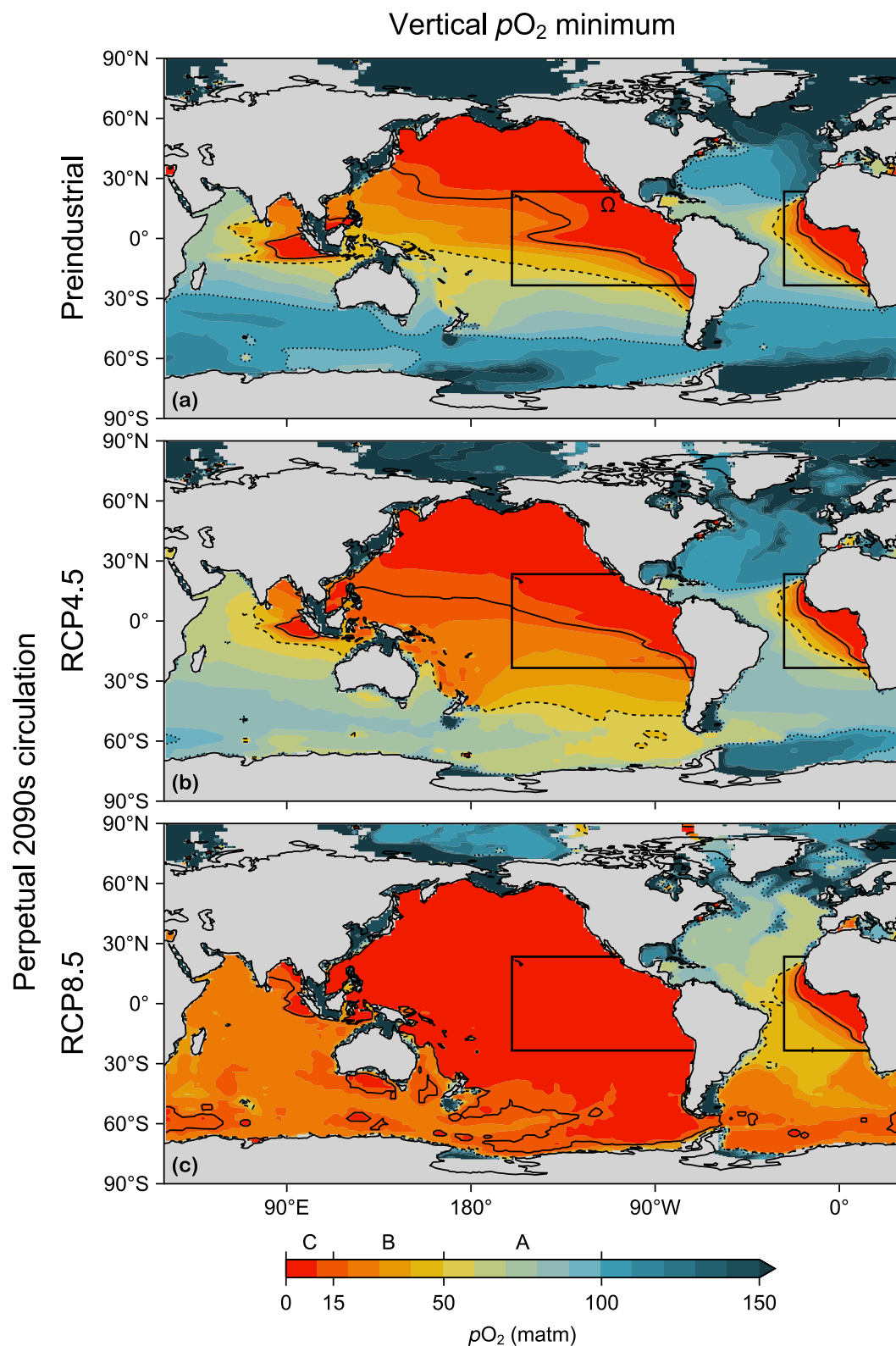


Figure 4. (a–c) Maps of the water-column minimum pO_2 for (a) the preindustrial state, (b) the perpetual-2090s RCP4.5 state, and (c) the perpetual-2090s RCP8.5 state. The dotted, dashed, and solid contour lines indicate the $pO_2 = 100$, 50, and 15 matm thresholds of hypoxia categories A, B, and C, respectively. Also indicated are the eastern tropical Pacific and Atlantic Ω regions over which our diagnostics are applied.

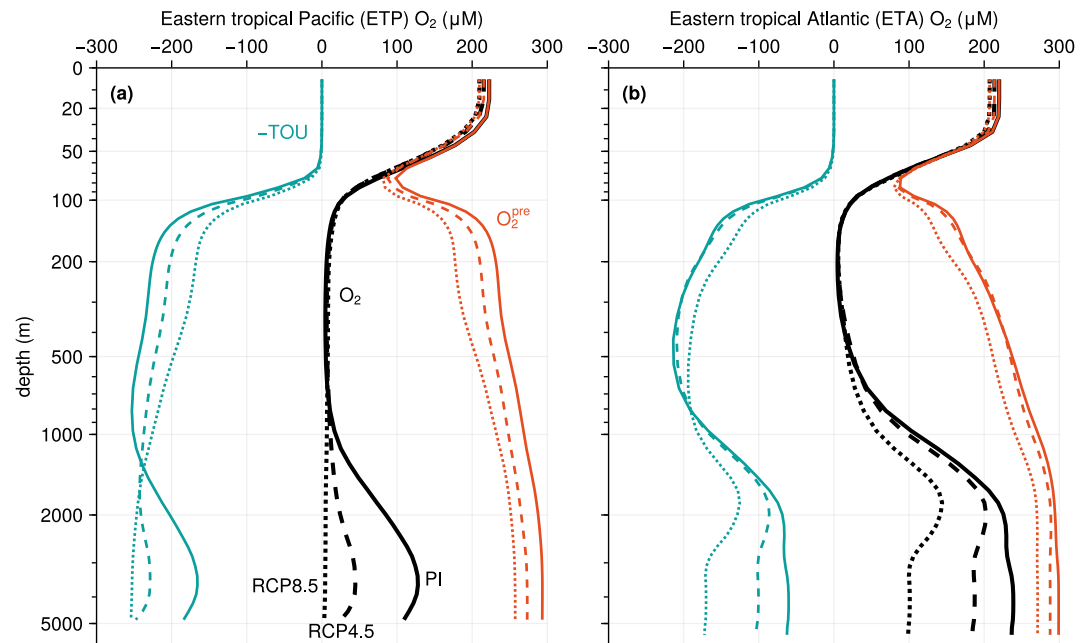


Figure 5. (a) Eastern tropical Pacific profiles of oxygen (O_2 , black), preformed oxygen (O_2^{pre} , orange), and true oxygen utilization (TOU, teal) for the preindustrial state (PI; solid line), the perpetual-2090s RCP4.5 state (dashed line), and the perpetual-2090s RCP8.5 state (dotted line). We show regenerated oxygen, $-TOU$, to show the effect of utilization on O_2 as additive. Note the nonlinear depth scale. (b) As (a) for the eastern tropical Atlantic (The eastern tropical Pacific and Atlantic regions are defined in Figure 4).

preindustrially deep mixed layer in these regions (see Figure C2 in Pasquier et al. (2023)) considerably increases surface residence times, allowing preindustrially undersaturated O_2 to become more saturated despite the decreased solubility (see Section 4.1 for caveats on the circulation model).

To analyze the drivers of deoxygenation in detail, we focus for definiteness on the eastern tropical Pacific (ETP, 23°S–23°N, east of 160°W) and eastern tropical Atlantic (ETA, 23°S–23°N, east of 27°W), as indicated in Figure 4. Figure 5 shows the average O_2 depth profiles in these regions and their decomposition into O_2^{pre} and TOU. In the preindustrial state, both the ETP and ETA are severely hypoxic in the depth range of 150–800 m and 150–400 m, respectively. In the perpetual-2090s steady states, we find small upper-ocean O_2 decreases of about 10 μM above 70 m, caused by a decrease in O_2^{pre} . Decreases in O_2^{pre} are approximately constant with depth below ~ 100 m, while ΔTOU changes sign at $\sim 1,500$ m in the ETP and at ~ 800 m in the ETA. Above ~ 500 m, the TOU decreases compensate almost perfectly for the O_2^{pre} decreases. Conversely, below $\sim 2,000$ m, TOU increases and O_2^{pre} decreases compound, resulting in strong deoxygenation, with deep ETP O_2 reduced to $\sim 25\%$ of its preindustrial levels for RCP4.5 and to a mere $\sim 5\%$ for RCP8.5. Deep ETA O_2 decreases are of similar magnitude, but O_2 levels are roughly 100 μM higher in all states owing to North Atlantic ventilation.

We now partition the changes ΔTOU and ΔO_2^{pre} into contributions from the key drivers, that is, into contributions from changes in circulation, respiration, and solubility (Section 2.5). For this purpose, we narrow our focus to the ETP only—similar mechanisms are at play in the ETA, but will not be discussed here for brevity. Guided by the shape of their profiles in Figure 5, we furthermore integrate over the upper ETP (above 500 m) and separately over the deep ETP (below 2,000 m) to summarize how different drivers dominate at different depths (For simplicity, we use the surface rather than the mixed- or euphotic-layer base as the top boundary of the upper ETP so that it occupies the same volume for all states). The resulting attribution of ΔTOU and ΔO_2^{pre} to their drivers is shown in Figure 6; we first discuss ΔTOU and then ΔO_2^{pre} .

3.2.2. Upper and Deep ETP Budgets of ΔTOU

The average TOU over a given region Ω is given by the global volume integral of the product of OUR with the upstream exposure time, $\Gamma_{\Omega}^{\uparrow}$ in steady state (see Section 2, Equation 2, and Figure 1). This allows us to decompose

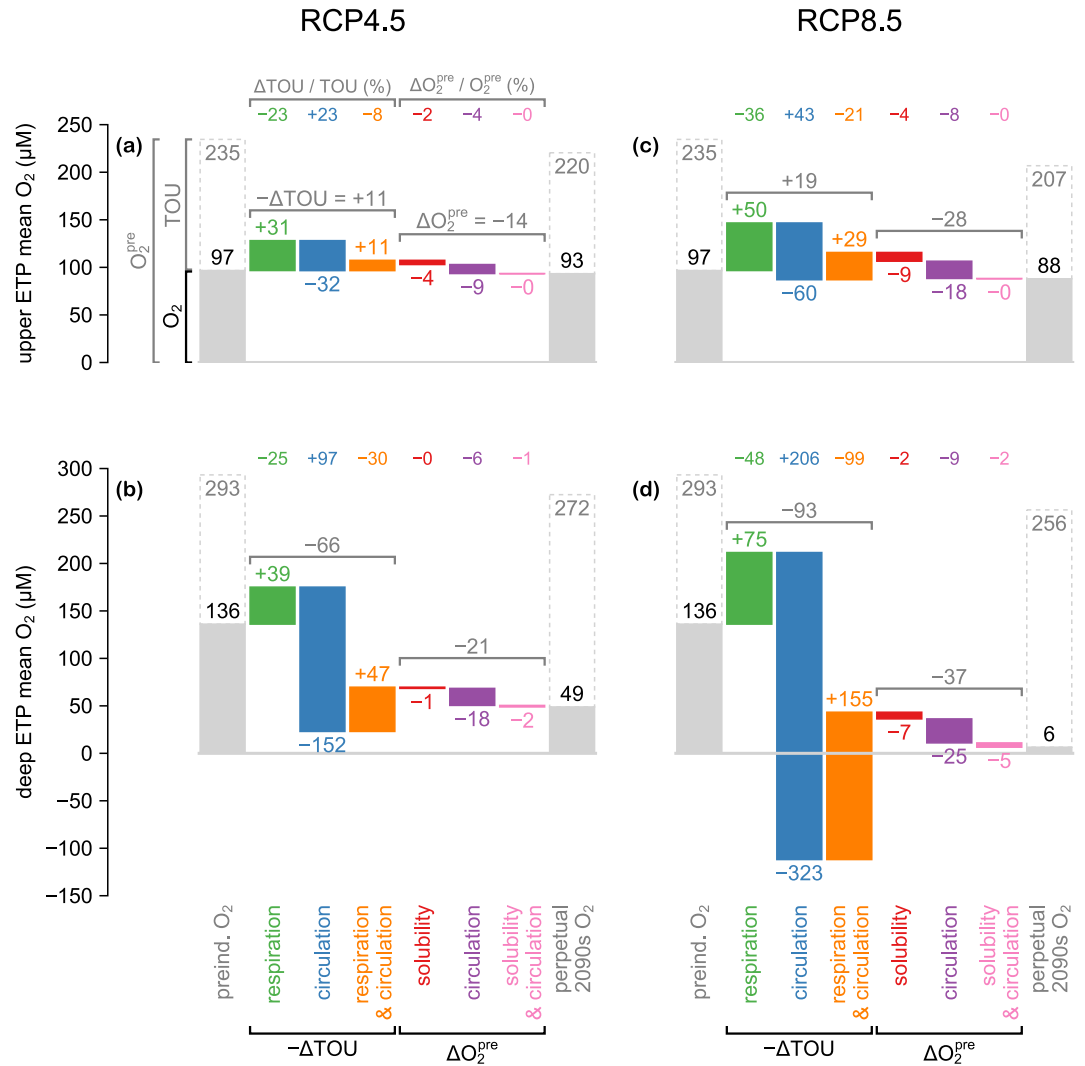


Figure 6. (a) ΔO_2 contributions for the upper ETP (0–500 m) for RCP4.5 plotted as a waterfall chart with the O₂ change from the preindustrial state (leftmost gray bar) to the perpetual-2090s state (rightmost gray bar) decomposed into contributions (colored bars) that start where the previous one ends. ΔTOU is decomposed according to Equation 3 into contributions from changes in respiration (green), circulation (blue), and their spatial covariance (orange). $\Delta\text{O}_2^{\text{pre}}$ is decomposed into contributions from solubility (red), circulation (purple), and their spatial covariance (pink). Percentage contributions to changes in TOU and O₂^{pre} are indicated at the top. (b) As (a) for the deep ETP (below 2,000 m). (c and d) As (a and b) for RCP8.5.

ΔTOU into contributions from changes in respiration, from changes in circulation, and from their spatial correlations, which we refer to as the “cross term” in Equation 3. These contributions are shown as the first three colored bars in each panel of Figure 6.

In general terms, Figure 6 shows that the global decline in respiration acts toward decreasing TOU (green bars; note that Figure 6 shows $\Delta\text{O}_2^{\text{reg}} = -\Delta\text{TOU}$), and hence increasing O₂ everywhere, as expected. Conversely, the slower 2090s circulation increases TOU (blue bars) by increasing the upstream exposure time, allowing respiration, albeit at a reduced rate, to act over longer times. The magnitude of the cross-term contributions to ΔTOU (orange bars) are generally on the same order as the circulation-only and respiration-only contributions, partly because of the large changes considered here. Note that the ΔTOU cross term acts toward increasing O₂ because ΔOUR and $\Delta\Gamma_{\Omega}^{\dagger}$ have opposite signs (negative contribution to ΔTOU). We now examine the drivers of TOU changes in detail for the upper and deep ETP.

For the upper ETP (Figures 6a and 6c), respiration-driven TOU reduction (green bar) is closely compensated by circulation-driven TOU increases (blue bar). This shows that in the upper ocean respiration is slower (driving TOU reductions of 23% and 36% for RCP4.5 and RCP8.5), but the slower circulation allows this respiration to act for longer (driving TOU increases of 23% and 43%). As the effects of respiration-only changes (green bars) and circulation-only changes (blue bars) nearly cancel, the overall TOU decrease is driven by the spatial correlation between respiration changes and circulation changes (orange bars). The concurrent increase of the circulation-only driven TOU and decrease of the respiration-only driven TOU must result in a negative cross term and hence in a TOU reduction, the precise magnitude of which depends on details of the underlying spatial patterns. The magnitude of the overall TOU decrease is about 8% for RCP4.5 and 21% for RCP8.5.

For the deep ETP, the circulation-only-driven ΔTOU (blue bars) dominates the other drivers with a magnitude that is roughly 5 times larger than for the upper ETP. In comparison, the magnitude of the respiration-only-driven ΔTOU (green bars) is only 30% and 50% larger for RCP4.5 and RCP8.5 than in the upper ETP. The respiration-driven decreases and circulation-driven increases in TOU again point to slower respiration acting for longer time. To quantify this, we calculated the upstream-exposure-time-weighted change in OUR and the OUR-weighted change in upstream exposure time to find that respiration slows by 25% for RCP4.5 and 50% for RCP8.5 but acts 2 times longer for RCP4.5 and 3 times longer for RCP8.5. For the deep ETP the cross terms (orange bars) are of the same order of magnitude as the respiration-only contribution (green bars), but the cross terms no longer dominate the overall TOU change as in the upper ETP. With all terms combined, the TOU of the deep ETP increases by 42% for RCP4.5 and by 59% for RCP8.5. A striking feature of these results is that, were respiration to be held constant at its preindustrial level, the ΔTOU contribution from the circulation slowdown alone (blue bars) is so strong that it would have the potential to remove the entire O_2 content of the deep ETP (filled gray bars) in the RCP4.5 scenario, and to do so more than two times over in the RCP8.5 scenario.

3.2.3. Upper and Deep ETP Budgets of $\Delta\text{O}_2^{\text{pre}}$

The preformed oxygen content of volume Ω is controlled by euphotic O_2 concentrations and by the amount of the Ω volume that is ventilated per unit area at the base of the euphotic layer, $\mathcal{V}_\Omega^{\downarrow}$ (see Section 2, Equation 4). While $\mathcal{V}_\Omega^{\downarrow}$ depends only on the circulation, euphotic O_2 concentration is determined by both solubility and circulation through the subtle balance between air–sea gas exchange and euphotic-zone residence time. However, decomposing euphotic O_2 into saturation and disequilibrium components, O_2^{sat} and O_2^{dis} , allows us to separate solubility from circulation effects (including their spatial correlation “cross term” in Equation 5) because euphotic O_2^{sat} is determined by in situ solubility only, while euphotic O_2^{dis} is predominantly determined by circulation. These contributions, volume integrated over either the upper or deep ETP, are also plotted as colored bars in Figure 6.

Reduced surface solubility reduces the preformed oxygen inventory of the ETP by just a few percent (red bars) even for the extreme RCP8.5 case, accounting for less than $\sim 30\%$ of the overall O_2^{pre} decrease in the upper and deep ETP. The bulk ($\sim 70\%$ or more) of the overall order-10% decline in preformed oxygen is instead driven by changes in circulation (purple bars). The cross terms (pink bars) between already relatively small solubility-only and circulation-only contributions are essentially negligible. The circulation-only driven reductions in O_2^{pre} due to $\Delta\mathcal{V}_\Omega^{\downarrow}$ represent re-arrangements in euphotic origin because the area integral of $\mathcal{V}_\Omega^{\downarrow}$, which equals the volume of Ω , is constant across all states. The decreases in the circulation-only contributions to $\Delta\text{O}_2^{\text{pre}}$ (computed with the preindustrial surface oxygen concentration) thus indicate a shift in ventilation pattern toward surface locations with lower oxygen concentration, that is, toward warmer latitudes with lower solubility (see also Figure B4). This equatorward shift in ventilation reduces the efficiency of the oxygen solubility pump and is the dominant driver of the decline in the preformed O_2 in both the upper and deep ETP.

It is interesting to note that regions with weaker ventilation have longer surface residence time and thus higher surface saturation, which can compensate for reduced solubility. In our perpetual-2090s states this occurs near the Weddell and Ross seas where the deep preindustrial mixed layer shoals dramatically thereby increasing surface residence and saturation, which overwhelm the effect of reduced solubility leading to increased surface oxygen concentrations.

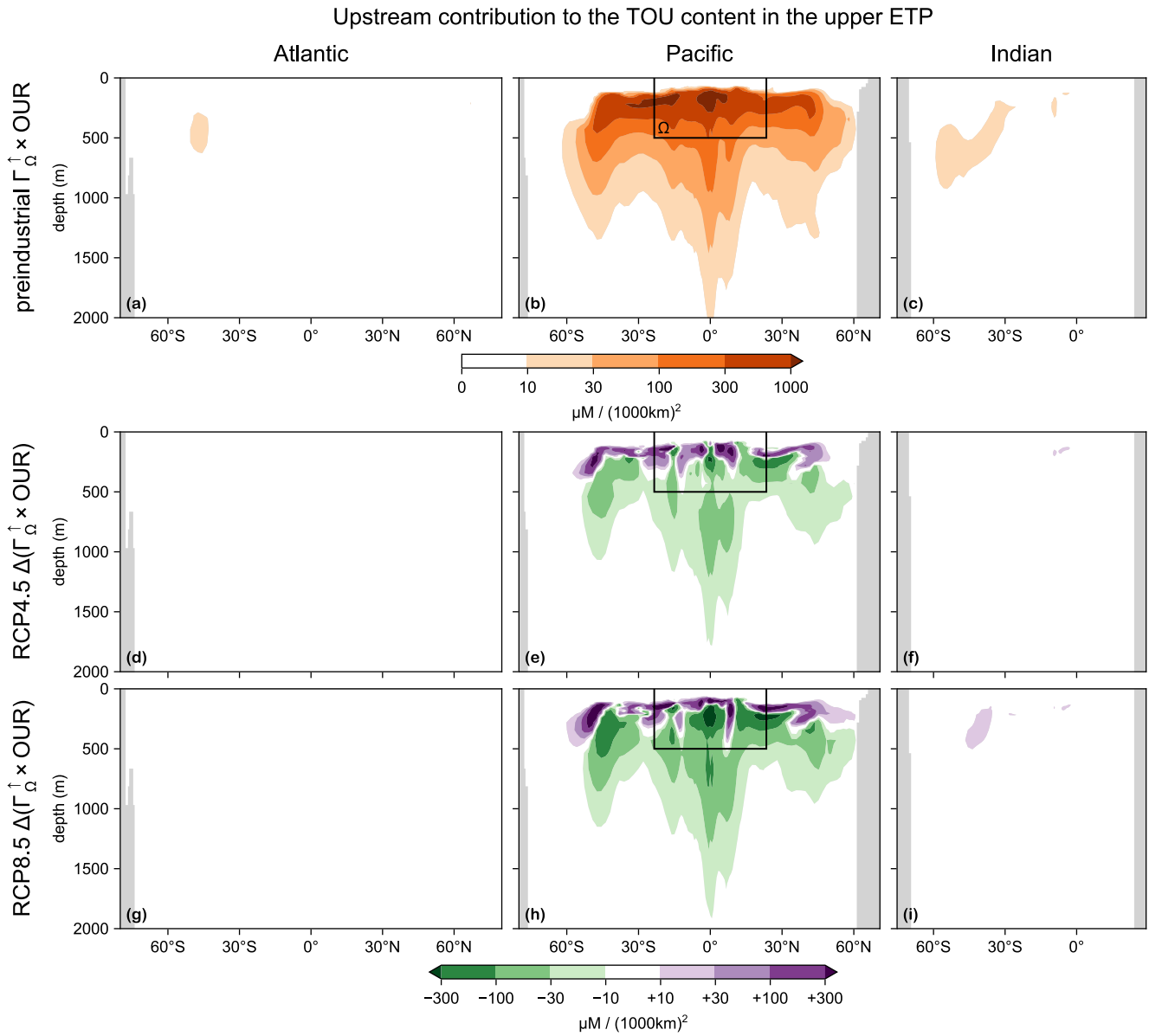


Figure 7. Preindustrial upstream contribution to the TOU in the upper ETP (0–500 m; indicated by the solid black line; subvolume Ω in our equations) as quantified by basin zonal integrals of $\Gamma_{\Omega}^{\uparrow} \times \text{OUR}$ normalized by the ETP volume for the Atlantic (a), Pacific (b), and Indian Ocean (c). (d–f) As (a–c) for the change from the preindustrial state to the perpetual-2090s state for the RCP4.5 scenario. (g–i) As (d–f) for RCP8.5. Note the nonlinear color scale and that the normalized zonal integrals plotted give the contribution per unit latitude–depth area.

3.2.4. TOU Changes in the ETP: Three-Dimensional Distribution of TOU Origin

Having quantified the globally integrated drivers of ETP deoxygenation, we now investigate their spatial distribution, beginning with the local contributions to TOU. The local contribution at point r to the TOU inventory of region Ω is given by the product $\Gamma_{\Omega}^{\uparrow}(r) \text{OUR}(r)$, which quantifies the origin of the TOU inventory, that is, the oxygen loss that occurred at r upstream of Ω . Figures 7 and 8 show the TOU origin for the upper and deep ETP, respectively. The zonally integrated TOU origin is plotted for the preindustrial state together with the corresponding changes for the perpetual-2090s states.

For the upper ETP (Figure 7), TOU originates almost exclusively in the Pacific, predominantly in thermocline waters across all non-polar latitudes, with peak contributions at a depth of ~ 200 m. Thus, there is significant oxygen loss within the upper-ocean circulation as it transports oxygen to the upper ETP. TOU in the upper ETP

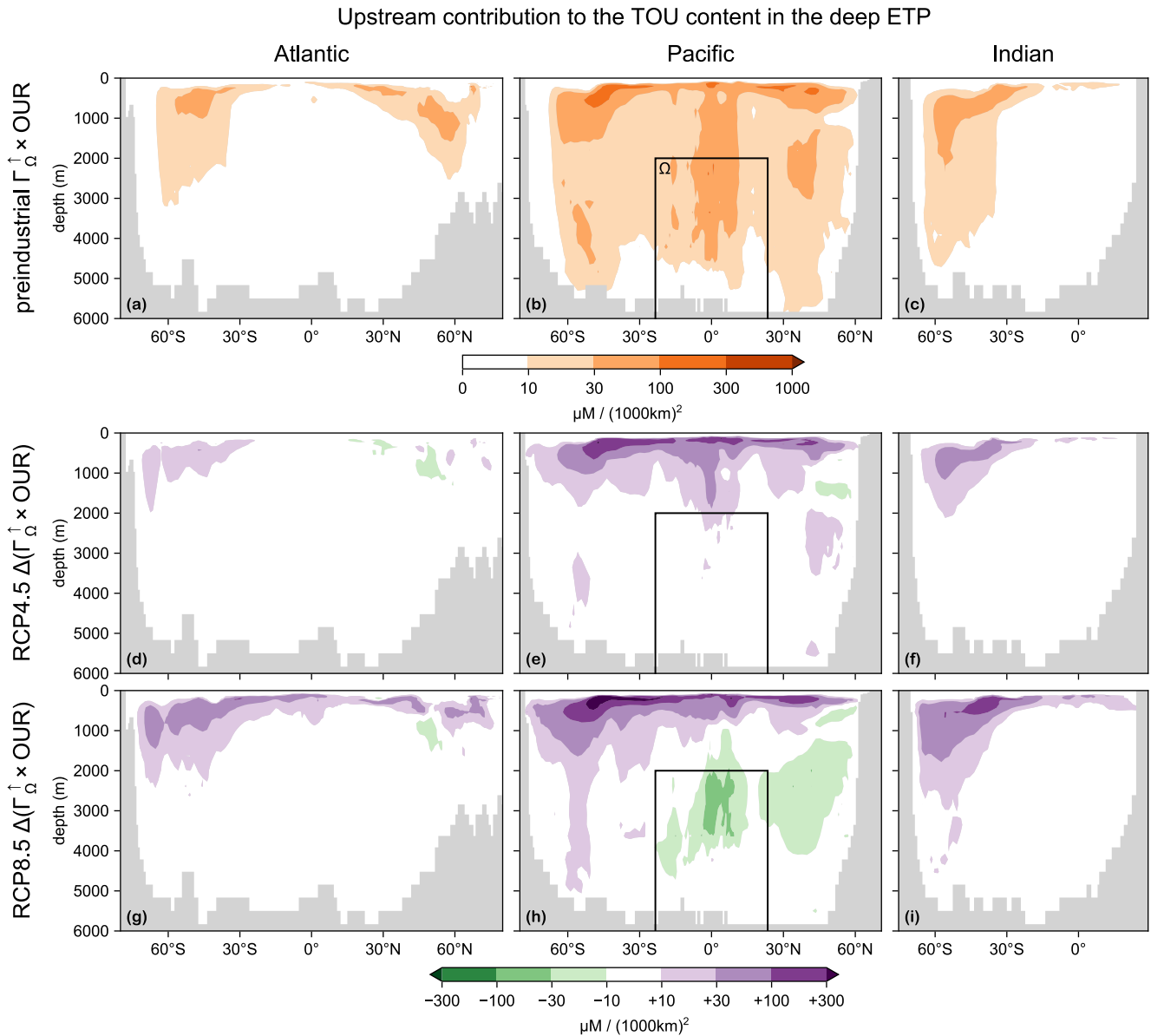


Figure 8. As Figure 7 for the deep ETP (below 2,000 m; indicated by the solid black line).

also originates at depths between 1,000 and 2,000 m at low and high latitudes, where upwelling old oxygen is intercepted by the bacterial respiration of abundant sinking organic matter beneath high productivity. For both RCP4.5 and RCP8.5, the change in TOU origin reveals a shoaling (upward shift) of the average location where oxygen bound for the upper ETP is lost. This shift presumably occurs because the slower 2090s circulation allows respiration to act for longer so that oxygen bound for the upper ETP is stripped out higher in the water column. The TOU origin below the thermocline at low and high latitudes decreases, presumably because of reduced biological productivity and subjacent respiration, as well as a lower O_2 content of the water that upwells there. The upward shift in TOU origin and reduced deep origin are thus both consequences of respiration removing oxygen sooner, that is, further upstream, during its transit from the euphotic zone.

For the deep ETP (Figure 8), TOU originates in every ocean basin. The Atlantic makes a 20% contribution and the Indian Ocean a 15% contribution, mostly at high latitudes known to ventilate the deep Pacific (e.g., Holzer et al., 2021). For all basins, the largest TOU origin lies in upper thermocline waters where most respiration occurs. Deeper TOU origin at high latitudes, and in the Pacific throughout the water column at low latitudes, occurs below

regions of vigorous biological production where respiration is high. The fact that the low-latitude tongue of oxygen loss in the Pacific lies partly above, and hence *down*-stream of the deep ETP, implies that either some O_2 is utilized as it mixes diffusively downward, or, more likely, that water destined to be carried by meridional overturning back to the deep ETP at depth has its oxygen stripped out in the upwelling branch of the overturning. Consistent with such an overturning pathway, local maxima of TOU origin occur in the mid-depth North Pacific and in the abyssal Pacific sector of the Southern Ocean.

The changes in the TOU origin of the deep ETP plotted in Figure 8 show a global increase and upstream intensification of the removal of oxygen destined for the deep ETP. For the RCP4.5-based perpetual-2090s state, the TOU origin increases mostly near the surface of the Pacific, South Atlantic, and southern Indian Ocean where it was already large in the preindustrial state. For RCP8.5, the TOU contributions are generally stronger and, unlike for RCP4.5, they also increase near the North Atlantic surface. However, in the old waters of the mid-depth North Pacific the TOU origin of the deep ETP actually decreases for RCP8.5, likely because of shifts in production, and hence respiration, away from the surface origin of these old waters so that less oxygen is stripped out of them.

3.2.5. Preformed Oxygen Changes in the ETP: Shifting Ventilation Patterns

Here we take a closer look at the geographic shifts in ventilation patterns that drive the decreased preformed oxygen content of the ETP. The amount of O_2^{pre} supplied to Ω from euphotic location r is quantified by the product $O_2(r) \mathcal{V}_{\Omega}^{\downarrow}(r)$, maps and zonal integrals of which are plotted in Figure 9 for the preindustrial state together with the changes for the perpetual-2090s states (Corresponding plots of $\mathcal{V}_{\Omega}^{\downarrow}$ by itself, shown in Figure B4, share strong similarities with Figure 9, underscoring that changes in ventilation patterns are the dominant driver of ΔO_2^{pre}).

For the upper ETP, the origin of preformed oxygen in the preindustrial state (Figure 9a) shows that while much oxygen comes from the overlying surface, a considerable fraction is supplied from Mode and Intermediate water-formation regions in the Pacific, and from deep-water formation regions in the Southern Ocean (Weddell and Ross Seas) and North Atlantic. For the deep ETP in the preindustrial state, the tropical and subtropical contributions are much weaker while contributions from the deep-water formation regions of the Southern Ocean and the North Atlantic are more important.

For the perpetual-2090s states, the largest decreases in preformed oxygen origin occur in the deep-water formation regions, particularly near the Weddell and Ross Seas. The supply of O_2^{pre} from south of 60°S declines by about 70% and 50% for the upper and deep ETP, respectively, for the RCP4.5 scenario, and almost completely shuts down for both the upper and deep ETP for RCP8.5. As discussed for Figure 6 and underscored by the similarity between Figures 9 and B4, this is dominantly due to circulation-driven changes in ventilation. Large-scale increases of the O_2^{pre} supply are most prominent in the subtropical gyres, which are more important oxygen sources for the ETP in our perpetual-2090s states.

4. Discussion

We investigated the deoxygenation of the ocean for idealized steady-state biogeochemistry in equilibrium with frozen-in-time physical ocean states. We used two ocean states averaged over the 2090s for the RCP4.5 and RCP8.5 scenarios and held constant in time for perpetuity, plus a corresponding 1990s steady state (“preindustrial” for short) for our analysis. To attribute the deoxygenation to its drivers, we focused on the eastern tropical basins (primarily in the Pacific) as these contain OMZs in the current ocean, and because their deoxygenation is typical of the large-scale steady-state response in our model. The key driving mechanisms were quantified by decomposing the oxygen changes into contributions from changes in surface solubility, ocean circulation, and oxygen utilization rates. Here we discuss important caveats of our approach and contrast our results with other work on ocean deoxygenation.

4.1. Caveats

A number of caveats must be kept in mind when interpreting our findings. Some caveats also apply to the nutrient and carbon cycles and have been previously discussed by Pasquier et al. (2023, 2024). Below we discuss the caveats specific to our analysis of deoxygenation.

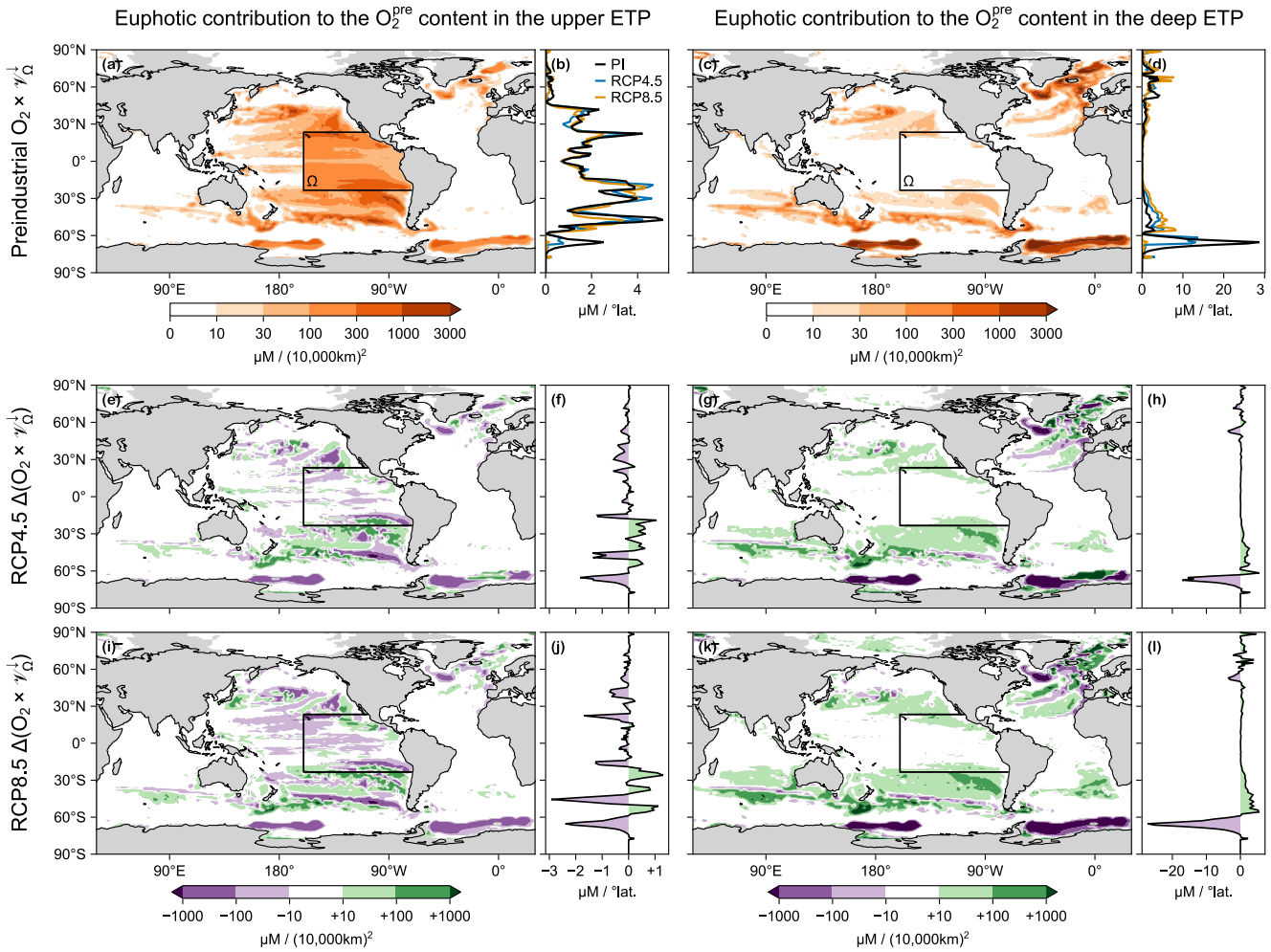


Figure 9. (a) Map and (b) zonal integral of the euphotic contribution to the mean O_2^{pre} in the upper ETP (subvolume Ω indicated by a solid black contour), as quantified by $O_2 \times V_{\Omega}^{\downarrow}$ normalized by the volume of Ω , in the preindustrial state. (c and d) As (a and b) for Ω the deep ETP. (e–h) As (a–d) for $\Delta(O_2 \times V_{\Omega}^{\downarrow})$ for the RCP4.5 perpetual 2090s. (i–l) As (e–h) for RCP8.5. Note the nonlinear color scale and that the contributions plotted are per unit horizontal area.

(i) The biogeochemical states analyzed here are steady and embedded in circulations that are frozen in time. By contrast, the real ocean circulation is currently slowing down and will continue to evolve for millennia even for fixed external forcing (e.g., Srokosz & Bryden, 2015). Given the ocean's wide range of transit times (e.g., Primeau, 2005), the circulation will keep changing well beyond the 21st century until deep convection, ventilation, and overturning eventually recover after a few millennia (e.g., Schmittner et al., 2008), which results in a different state from those considered here. Thus, neither the oxygen distribution nor the circulation and thermodynamic ocean state are expected to be anywhere near steady by the end of the 21st century (e.g., Shaffer et al., 2009). Our biogeochemical states therefore cannot be interpreted as predictions of the future. In particular, by allowing oxygen to fully equilibrate with frozen circulations that feature strongly weakened Southern Ocean ventilation and bottom-water formation, our idealized steady states exhibit intense abyssal deoxygenation that will certainly not be manifest by 2100. However, our analysis does provide a glimpse into the possible mechanisms that could shape the oxygen response on its very longest timescales. Furthermore, our steady-state framework accounts for neither natural variability nor seasonality. In particular, we cannot capture the effects from seasonally covarying changes in biology, physics, and thermodynamics, which play a significant role in the seasonality of oxygen in the upper few hundred meters as seen in both observations and models (see, e.g., Espinoza-Morriberón et al., 2021; Graco et al., 2017; Jin et al., 2007; Pitcher et al., 2021, to cite a few).

- (ii) In terms of precise quantitative values, our results are specific to the circulation of the parent climate model. The unrealistically deep Southern Ocean mixed layer of the preindustrial state inherited from the parent ACCESS1.3 model (Bi et al., 2013), and its shoaling in the future, leave a pronounced imprint on our results. However, unrealistically deep mixed layers in the polar Southern Ocean are a feature common to virtually all CMIP5 models (e.g., de Lavergne et al., 2014), in which AABW is formed by deep convection compensating for unresolved sinking of Antarctic shelf waters. Importantly, the qualitative deoxygenation mechanisms identified here for idealized steady-state oxygen in frozen-in-time 2090s circulation are unlikely to depend on which particular CMIP5 model is used to generate the idealized state. Most CMIP5 models share the qualitative feature of declining Southern Ocean ventilation and shoaled mixed layers at the end of the 21st century (e.g., de Lavergne et al., 2014; Heuzé et al., 2015; Kwiatkowski et al., 2020). These are both critical circulation changes for producing intense equilibrated deoxygenation when the circulation is frozen in time. Another relevant feature of the ACCESS1.3 parent model is that it does not include melting land-fast ice sheets, which impact Southern Ocean ventilation (Chen et al., 2023; Li et al., 2023). If meltwater from ice sheets were included, we would expect a stronger reduction in Southern Ocean ventilation (Purich & England, 2023; Purich et al., 2018), which we would expect to strengthen the circulation-change contribution to deoxygenation. We emphasize, however, that the realism of the mechanism that produces reduced Southern Ocean ventilation and throttled bottom-water formation is not important for our idealized deoxygenation scenarios. Any circulation with these features that is frozen in time would likely produce intense abyssal deoxygenation similar to what we document here.
- (iii) In terms of quantitative detail, our results are also specific to the PCO2 biogeochemistry model that was used (Pasquier et al., 2023). PCO2 was designed to be relatively simple and does not explicitly represent every mechanism at play in the real ocean. Potentially important missing mechanisms include feedbacks from the nitrogen cycle, which are linked to oxygen through denitrification and nitrification. Denitrification, which is only modeled implicitly in PCO2 (see Equation 1), is important because anaerobic respiration in low oxygen environments acts as an effective oxygen source. Conversely, nitrogen fixation and nitrification, which produce nitrite and nitrate by consuming oxygen, are not represented at all in PCO2. Effects from the nitrification–denitrification imbalance on the oxygen cycle, expected to contribute about two thirds of a ~ 6% increase in the global O₂ inventory by the year 8000 (Oschlies et al., 2019), are therefore not captured in our model. However, we note that this imbalance is expected to be dominated by denitrification (which is parameterized in PCO2) and remains secondary for the first few centuries of sluggish circulation until about the year 5000 when the overturning circulation recovers.

4.2. Relation to Previous Work

Because our analysis is framed for idealized steady-state biogeochemistry in equilibrium with frozen-in-time circulations, we do not expect a detailed match with previous studies based on transient simulations. We do, however, expect similarities with simulations that last long enough for the effect from slow processes to manifest. In particular, this includes processes mediated by the slowdown of the deep ocean circulation, which is the dominant driver of deoxygenation in our analyses and operates on multi-centennial timescales (e.g., Primeau, 2005), with effects that will not have asserted themselves by the end of the 21st century in transient simulations of oxygen (e.g., Moore et al., 2018). However, the relatively more sluggish ocean state predicted for the next few centuries will likely only be temporary. A more vigorous circulation is expected to return after several millennia as deep ocean temperatures equilibrate (e.g., Frölicher et al., 2020; Schmittner et al., 2008). The more vigorous circulation and stronger Southern Ocean ventilation predicted for a future steady state of the ocean could thus result in the opposite response found here for our perpetually warmer and slower ocean states. In particular, in the very long term, deep preformed O₂ could actually increase despite a globally warmer ocean because of a poleward shift in the origin of deep oxygen. We therefore expect our results to be most relevant to predictions for a few centuries into the future before a more vigorous circulation re-establishes. We also note that differences in biogeochemistry, in ocean circulation, in scenarios and forcings, and so on, further complicate quantitative comparisons.

The very intense deoxygenation seen here at depth is driven by circulation changes that act in perpetuity, while corresponding effects in transient simulations have not fully developed by 2100. Thus, our results on deoxygenation are generally different in magnitude from what is seen in transient simulations, with very dramatic differences in the deep ocean. For the upper ocean, Kwiatkowski et al. (2020) reported a (10 ± 2) % decline in

100–600 m deep oxygen across CMIP5 models and a (13 ± 5) % decline across CMIP6 models for RCP8.5 and SSP5-8.5, respectively, compared to the $\sim 20\%$ decline for our RCP8.5-based perpetual-2090s steady state (CMIP6 uses the “Shared Socioeconomic Pathway” (SSP) classification (Riahi et al., 2017) where SSP5-8.5 nominally matches RCP8.5 (Arias et al., 2021)). Similarly, for RCP4.5, Kwiatkowski et al. (2020) reported a $6 \pm 3\%$ decline for CMIP5 and a $8 \pm 4\%$ decline for CMIP6, compared to a $\sim 7\%$ decline in this study for the same scenario. Near the sea floor, Kwiatkowski et al. (2020) reported a weak but consistent $6 \pm 2\%$ oxygen decline across CMIP6 models and scenarios, in stark contrast to the $\sim 40\%$ and $\sim 80\%$ decline in the abyss for our RCP4.5- and RCP8.5-based states, respectively. The hypoxic volumes in our perpetual-2090s states are thus dramatically larger than the predictions of a moderate $\sim 10\%$ expansion in mild hypoxia and a contraction of the OMZ core (e.g., Busecke et al., 2022; Gnanadesikan et al., 2012).

Longer-term transient simulations in principle allow for closer comparisons with our steady-state biogeochemistry embedded in frozen-in-time circulations but the recovery of the transient ocean circulation intervenes before the long-term effects of circulation slowdown can fully develop. Running a climate model with $p\text{CO}_2$ at three times its preindustrial level from 2100 onward, Matear and Hirst (2003) reported a $\sim 30\%$ decline in O_2 below 4,000 m by 2700. This O_2 decline is larger than those estimated for 2100 but still far from the corresponding 80% decline of our RCP8.5 perpetual-2090s state because the circulation effects on O_2 are not fully developed as evidenced by a deep O_2 trend that remains strongly negative by 2700. Matear and Hirst (2003) report spatial patterns that are similar to our steady-state responses, with intense O_2 declines in the deep Southern Ocean driven by decreased ventilation. However, the simulation by Matear and Hirst (2003) was not continued beyond 2700, which is roughly when the circulation is expected to start recovering. In a multimillennial double- $p\text{CO}_2$ simulation, Frölicher et al. (2020) find a 700-year decline in O_2 mostly below 2,000 m accumulating to a $\sim 10\%$ loss globally (compared to 40% for our RCP4.5 perpetual-2090s state) before O_2 slowly increases again over multiple millennia driven by the recovery of Southern-Ocean ventilation. In another multimillennial simulation with atmospheric $p\text{CO}_2$ reaching almost 2,000 μatm around year 2300 and slowly declining to $\sim 1,200$ μatm over the next five millennia, Oschlies et al. (2019) find an O_2 decline of $\sim 25\%$, also reached around year 2700, before O_2 levels increase again with the recovering overturning circulation.

Our analyses differ from previous studies by attributing deoxygenation to specific mechanisms, in particular by cleanly separating out the role of circulation changes. In our work here, solubility alone accounts for less than 10% of the global O_2 decline, which is lower than what is estimated for the transient 2100 ocean. Its idealized framework notwithstanding, our analysis of the role of solubility changes suggests that previous studies potentially overestimate the solubility contribution. Studies that infer the solubility contribution from a residual, typically between a climate-change simulation and a similar simulation with the solubility fixed to preindustrial values (e.g., Matear & Hirst, 2003), unintentionally include effects from changes in ventilation patterns (which should be attributed to circulation change) because the residual includes spatial correlation (“cross”) terms, which we estimate to be order 20% for our steady states in frozen-in-time circulations. Approximations based on heat flux generally overestimate the contribution from solubility changes because they assume complete saturation (e.g., 20%–30%; Bopp et al., 2002; Palter & Trossman, 2018). Solubility-change contributions quantified through an abiotic/preformed O_2 tracer are generally overestimated yet more (e.g., 30%–50%; Oschlies, 2021; Oschlies et al., 2019) because the preformed tracers respond to both saturation and circulation changes. Similarly, solubility contributions quantified directly by the change in saturation concentration as a function of in situ temperature and salinity are overestimated even more (e.g., 40%–70%; Frölicher et al., 2020). Only studies that perturb surface solubility alone in an otherwise unperturbed preindustrial state can provide unbiased estimates. Such unbiased estimates include, for example, the 15%, 25%, and 35% estimates by Matear et al. (2000), Bopp et al. (2002), and Plattner et al. (2001), respectively, the higher estimates likely being due to models with smaller changes in Southern Ocean ventilation.

5. Conclusions

We quantified the drivers of large-scale ocean deoxygenation for idealized steady-state biogeochemistry embedded in perpetual-2090s ocean states based on RCP4.5 and RCP8.5 ACCESS1.3 simulations. Our analysis is idealized because we allowed oxygen to fully equilibrate with a perpetually warmer and slower ocean, which is in stark contrast to transiently evolving biogeochemistry embedded in a more realistic dynamically changing circulation. Changes in biogeochemistry were evaluated relative to a steady preindustrial state and analyzed for the eastern tropical Pacific (ETP), which contains the largest hypoxic volume. We partitioned changes in TOU and

performed oxygen into their drivers, that is, into contributions from changes in circulation, respiration, solubility, and their interactions (cross terms).

To quantify the drivers of deoxygenation, we employed novel diagnostic methods that leveraged the steady-state nature of our idealized biogeochemistry. Key to our being able to isolate—for the first time—the role of circulation changes in driving deoxygenation is the conceptually novel upstream exposure time, a circulation timescale that controls the oxygen deficit of a given subvolume Ω of the ocean. Specifically, it is the time for which the oxygen that is “missing” from Ω was exposed to upstream respiration. The upstream exposure time thus provides the precise connection between TOU and OUR (Holzer, 2022) and, as shown here, the precise link between ventilation volume and preformed oxygen. In essence, the upstream exposure time, which is a function of advective–diffusive transport, traces TOU and preformed oxygen back in time to their origin.

Our main conclusions are as follows:

1. Keeping the 2090s ocean state frozen in time leads to steady-state oxygen distributions characterized by intense global-scale deoxygenation at depth. Global oxygen inventories decline by 30% and 60% for the RCP4.5 and RCP8.5 scenarios, respectively. For the extreme RCP8.5 case, Pacific abyssal waters become severely hypoxic ($pO_2 \leq 15 \mu\text{M}$) over the entire basin, while Atlantic and Indian Ocean abyssal waters become mildly hypoxic ($pO_2 \leq 100 \mu\text{M}$) everywhere. The extent of hypoxic regions in the upper ocean changes remarkably little in our more poorly ventilated perpetual-2090s states, owing to decreased preformed oxygen being compensated by reduced TOU.
2. For our idealized steady states, intense abyssal TOU increases are dominantly driven by the perpetual 2090s circulation being slower, thus allowing respiration to act over longer times. Modest upper-ocean TOU decreases are characterized by close compensation between respiration-only and circulation-only effects. Specifically, in the deep ETP, TOU increases of 50% for RCP4.5 and 100% for RCP8.5 are driven by 2–3 times longer upstream exposure to respiration, which overwhelms the decline in respiration rates. In the upper ETP, TOU decreases by about 10%. Thus, despite the global decline in respiration rates, the permanently slower circulation of our idealized states drives intense deoxygenation at depth and prevents increased oxygenation in the upper ocean.
3. In our idealized perpetual-2090s states, preformed oxygen declines virtually everywhere driven mostly by shifts in ventilation patterns, rather than by the decrease in solubility due to warmer sea-surface temperatures. More than 70% of the decline in preformed oxygen is driven by its surface origin shifting away from high latitudes toward lower latitudes, where warmer waters hold less oxygen. In situ warming-driven solubility reductions by themselves, at fixed circulation, reduce preformed oxygen by only $\sim 30\%$ in the upper ETP and by less than 20% in the deep ETP, accounting for less than 10% of the overall deoxygenation. Thus, while preformed oxygen is often thought to decrease because of warming-driven reduced solubility (e.g., Couespel et al., 2019; Oschlies, 2021; Oschlies et al., 2019; Palter & Trossman, 2018), our analysis reveals that, at least when the 2090s ocean state is maintained in perpetuity, the change in ventilation pathways is the dominant driver.

Our results show that, for our idealized states, circulation change is the key driver of deoxygenation. What the precise contribution of circulation change will be in the future ocean remains an open question. Our analysis suggests that to understand the fate of oxygen in the ocean, it is important to carefully quantify ventilation patterns and key ocean circulation timescales. Of particular importance is the upstream exposure time which is a key control on both preformed oxygen and TOU. For steady state, the necessary computations can efficiently be performed by building and using the associated transport matrices as was done here, and which we hope will become a more widely adopted practice. For time-evolving states, the analysis becomes significantly more complex, and extending our work to a dynamically changing oxygen cycle is left to the future.

Appendix A: Model–Observations Comparisons

Figure A1 shows the basin zonal-mean pO_2 for the preindustrial state of our model and for the GLODAPv2 observations, along with the corresponding mismatch. The unrealistically deep mixed layers of the Southern Ocean in the parent model manifest as overestimated pO_2 in the Atlantic and Pacific south of 60°S. Other

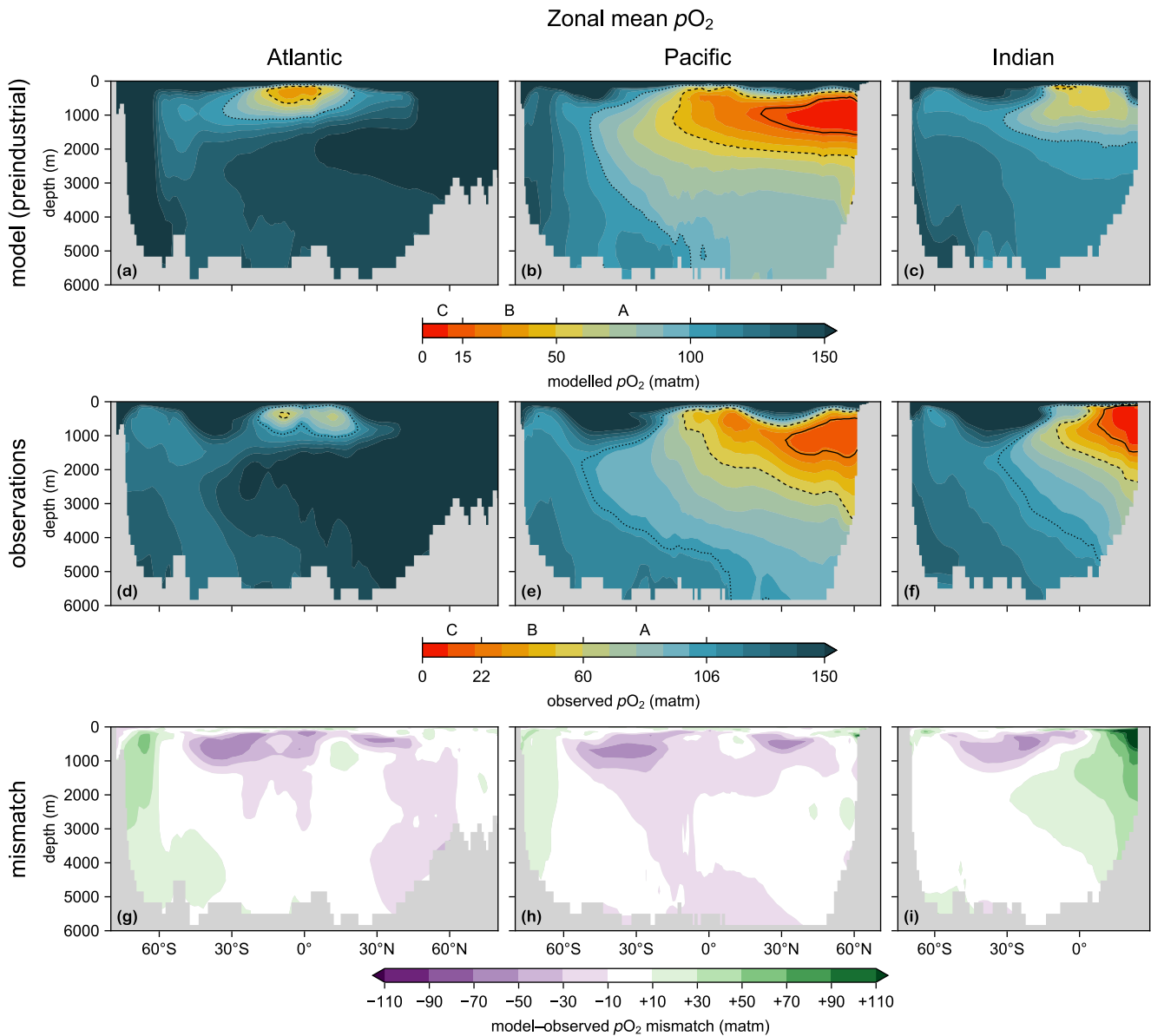


Figure A1. (a) Atlantic, (b) Pacific, and (c) Indian Ocean zonal mean pO_2 for the preindustrial state. The dotted, dashed, and solid contour lines indicate the thresholds of hypoxia categories A, B, and C, respectively (which are different for model and observations; see Section 2.6). (d–f) As (a–c) for observations. (g–i) As (a–c) for the model–observations mismatch. The Atlantic basin excludes the Gulf of Mexico and the Caribbean, and the Pacific basin excludes the Sea of Japan so that the zonal means are more cleanly interpretable.

systematic model biases are visible, for example, in the northern Indian Ocean, where PCO_2 overestimates pO_2 , and in the tropical and subtropical upper Atlantic and Pacific, where PCO_2 underestimates pO_2 .

Figure A2 shows the areal extent of each hypoxia category in each ocean basin as modeled for the preindustrial state and as captured by the GLODAPv2 observations. The extent of the Atlantic and Pacific hypoxic areas is generally overestimated, while the extent of the Indian-Ocean hypoxic areas is generally underestimated particularly at depth, consistent with Figure A1. We note that the pO_2 thresholds used are different for model and observations as they were adjusted for the model so that the global hypoxic volume for a given category is the same for the model as for GLODAPv2 (Section 2.6) (Note that the global match does not guarantee matching volumes within a given basin).

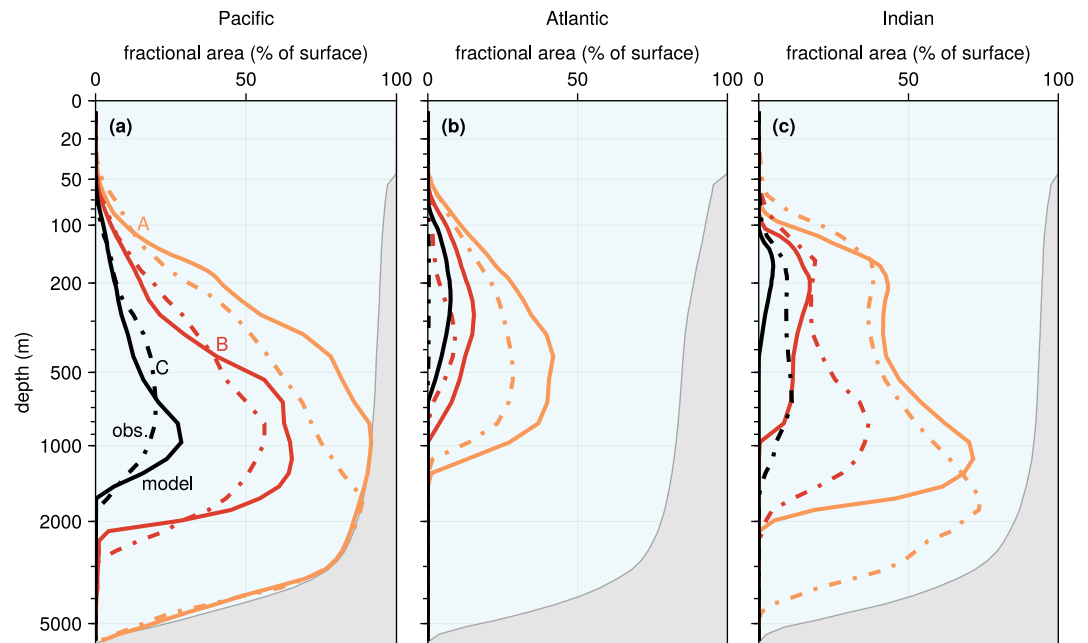


Figure A2. (a) Pacific depth profiles of the spatial extent of mild (A, orange), intermediate (B, red), and severe hypoxia (C, black) for the modeled preindustrial state (model; solid lines) and the observations (obs.; dash-dotted lines). (b) As (a) for the Atlantic. (c) As (a) for the Indian Ocean (The gray shading represents the seafloor). Note the nonlinear depth scale and that the pO_2 thresholds used for model and observations are different (see Section 2.6).

Figure A3 shows the geographic distribution of hypoxic waters as quantified by the water-column minimum of pO_2 for the preindustrial model state and for the GLODAPv2 observations. While the large-scale patterns seen in the observations are captured by the model, there are significant mismatches. The underestimated pO_2 in the Pacific and Atlantic manifest as OMZs (hypoxia category C) that are larger than observed. The model places the Indian Ocean OMZ southeast of western Indonesia while observations show it to occur in the Bay of Bengal and in the Arabian Sea.

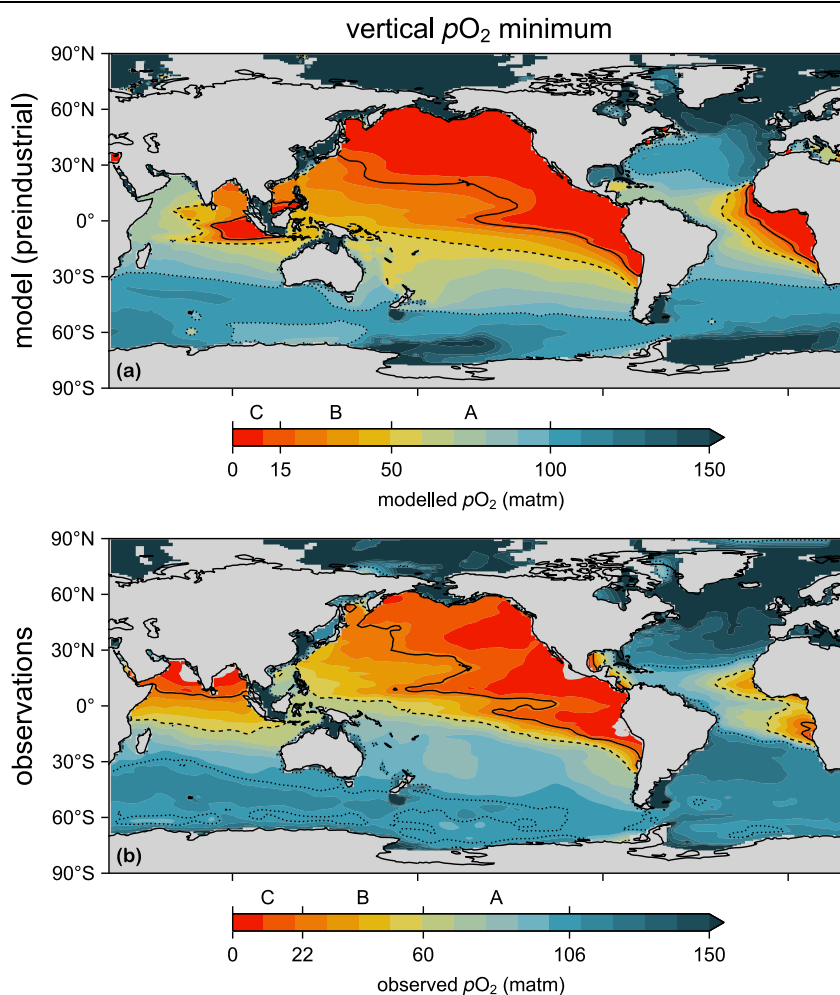


Figure A3. (a and b) Maps of the water-column minimum pO_2 for (a) the modeled preindustrial state and (b) observations. The dotted, dashed, and solid contour lines indicate the thresholds of hypoxia categories A, B, and C, respectively (which are different for model and observations; see Section 2.6).

Appendix B: TOU and O_2^{pre} : Patterns and Drivers

The left plots of Figure B1 show the Pacific zonal mean O_2^{pre} for the preindustrial state and the corresponding changes for the perpetual-2090s states. Near the surface, O_2^{pre} is higher in cold waters with greater oxygen solubility, and in the interior O_2 traces out (water) ventilation pathways. In the perpetual-2090s states, preformed O_2 declines almost everywhere and more strongly at depth, except in the surface Southern Ocean above ~ 200 m.

The right plots of Figure B1 show zonal mean TOU, which increases progressively as water traverses sinking organic matter where respiration strips out oxygen. TOU is generally largest at depths of about 500–1,500 m in the preindustrial state, and increases significantly at depth in the perpetual-2090s states. TOU and its changes are governed by both oxygen utilization rates (OUR) and upstream exposure times, shown below.

OUR, shown in the left plots of Figure B2, is generally surface intensified by several orders of magnitude as OUR is tightly linked to nutrient and carbon remineralization which attenuates quickly with depth. In our perpetual-2090s states, biological production and OUR decline globally though they are some local increases, mostly owing to spatial shifts in the nutrient supply. However, the effect of changes in OUR on O_2 is modulated by the time over which oxygen is exposed to respiration, discussed next.

The zonal-mean upstream exposure time $\Gamma_{\Omega}^{\uparrow}(r)$ is shown in Figure B2 for the case where the interior volume Ω of interest is either the upper ETP (middle plots) or deep ETP (right plots). Because in steady state the upstream

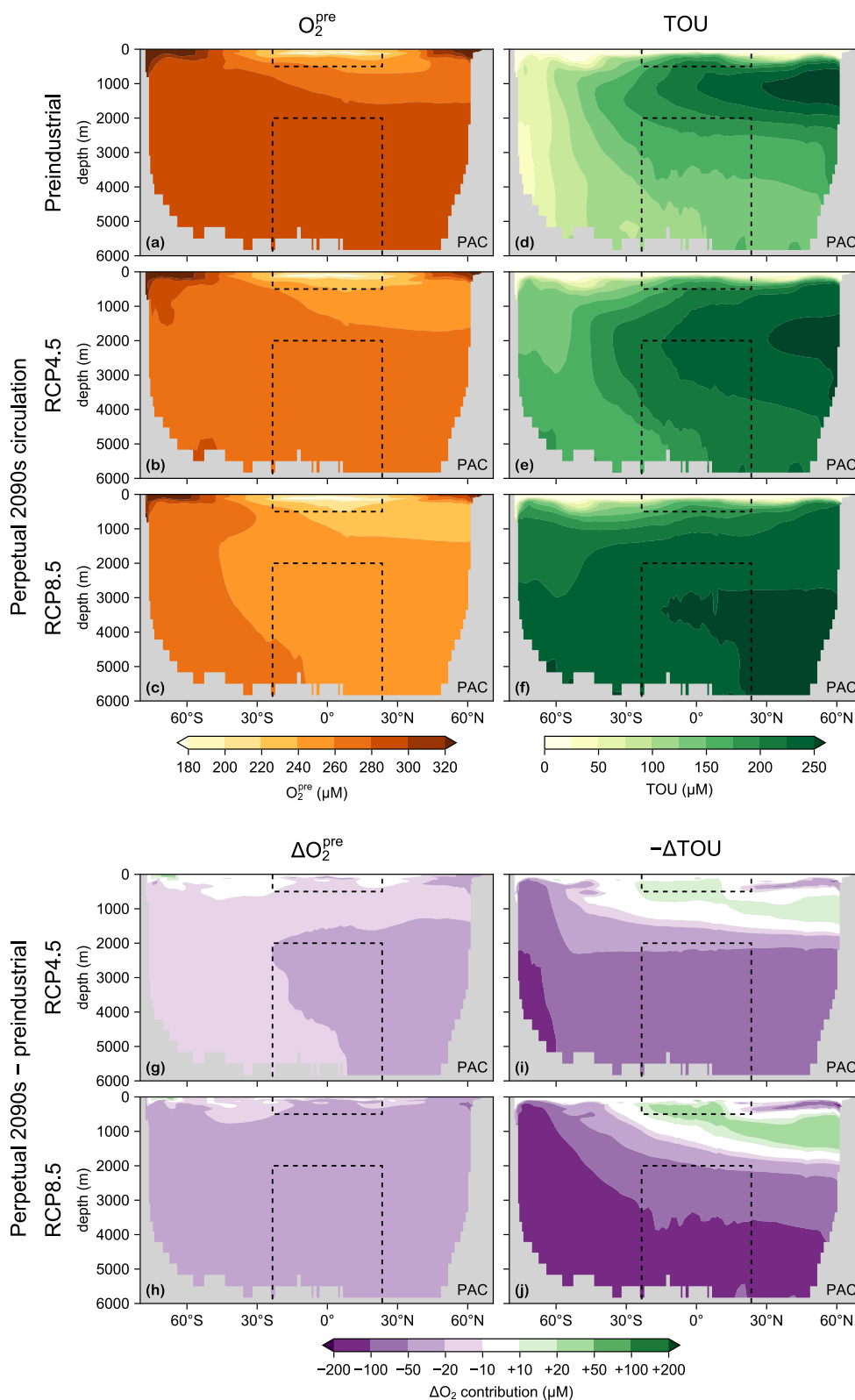


Figure B1. (a) Pacific zonal mean O_2^{pre} for the preindustrial state. (b and c) As (a) for the perpetual-2090s states (based on RCP4.5 and RCP8.5). (d–f) As (a–c) for TOU. (g–j) ΔO_2^{pre} and ΔTOU for RCP4.5 and RCP8.5. Dashed lines indicate the upper and deep ETP regions. Note the nonlinear color scale and that the Sea of Japan has been excluded so that these zonal means are more cleanly interpretable.

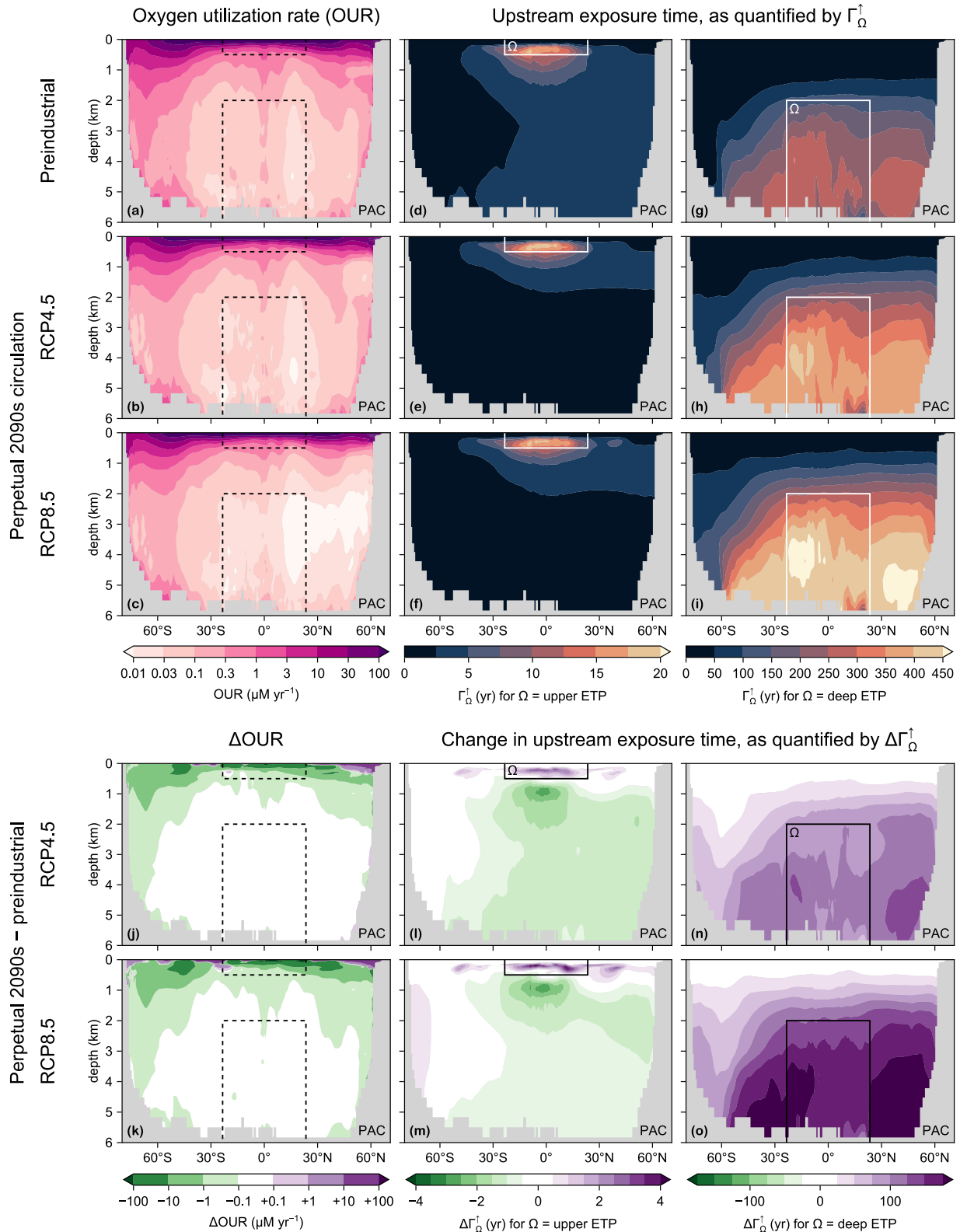


Figure B2. (a) Pacific zonal mean OUR for the preindustrial state. Dashed lines indicate the upper and deep ETP regions (Ω 's). (b and c) As (a) for the perpetual-2090s states (RCP4.5 and RCP8.5). (d–f) As (a–c) for the upstream exposure time Γ_{Ω}^{-1} of the upper ETP (above 500 m; solid white line). (g–i) As (d–f) for the deep ETP (below 2,000 m). (j and k) As (b and c) for ΔOUR . (l–o) As (e, f, h, i) for $\Delta\Gamma_{\Omega}^{-1}$. Note the nonlinear color scales and that the Sea of Japan has been excluded so that these zonal means are more cleanly interpretable.

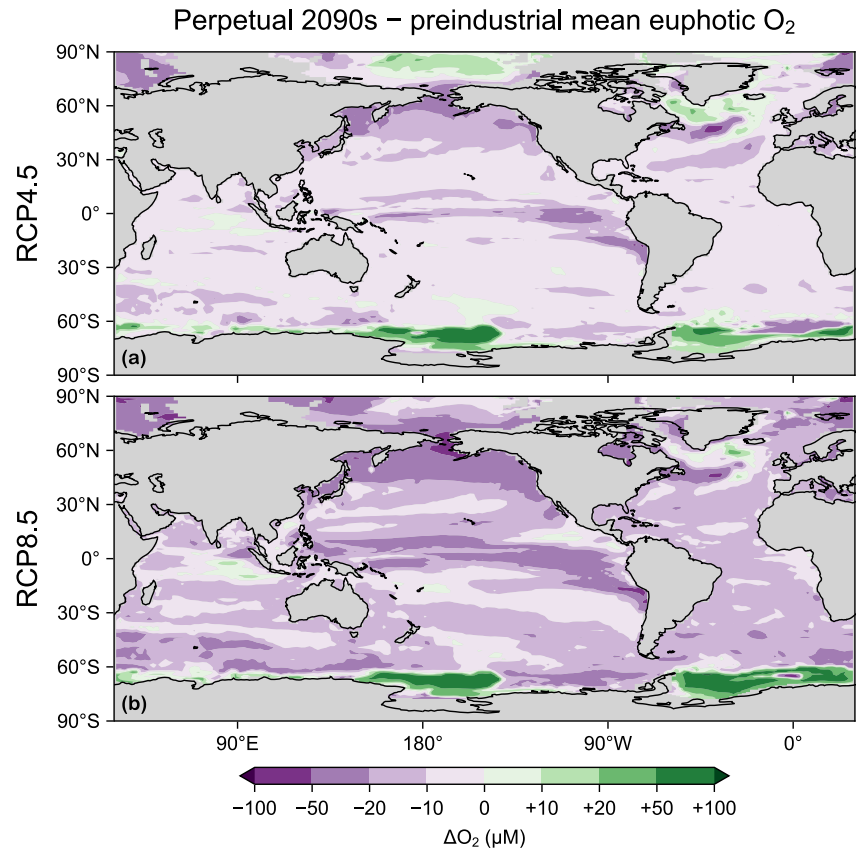


Figure B3. (a) Change in the euphotic-mean O₂ between the preindustrial state and the perpetual-2090s state for the RCP4.5 scenario. (b) As (a) for RCP8.5. Note the nonlinear color scale.

exposure time is also $\Gamma_{\Omega}^{\uparrow}(r)$, the time that water at r will spend in Ω , its magnitude approximately scales with the volume of Ω . Furthermore, because the deep circulation is much more sluggish than in the wind-driven thermocline, upstream exposure times are shorter for the upper ETP (less than ~ 20 years) than for the deep ETP (up to ~ 450 years). $\Gamma_{\Omega}^{\uparrow}$ is generally larger close to Ω and decreases with distance from Ω . Qualitatively, $\Gamma_{\Omega}^{\uparrow}$ can be thought of as a path selector roughly akin to the concentration of fluid elements destined to pass through Ω before exposure to the euphotic zone. Thus, $\Gamma_{\Omega}^{\uparrow}$ is shorter further away from Ω because more of the water there will be reexposed to the euphotic zone before it has a chance to pass through Ω .

In the perpetual-2090s states, a slower circulation tends to increase $\Gamma_{\Omega}^{\uparrow}$, but altered ventilation pathways can also reduce $\Gamma_{\Omega}^{\uparrow}$ (lower middle and right plots of Figure B2). For the deep ETP, the circulation slowdown drives strong $\Gamma_{\Omega}^{\uparrow}$ increases throughout the deep Pacific north of the Southern Ocean. By contrast, for the upper ETP, $\Gamma_{\Omega}^{\uparrow}$ increases above 500 m, but decreases in the Pacific below the thermocline north of $\sim 30^{\circ}\text{S}$. These decreases are likely because the surface ocean becomes more isolated in our perpetual-2090s states (Pasquier et al., 2024), reducing the flow of mid-depth, low-latitude waters through the upper ETP on their way back to the surface. Conversely, slight increases in $\Gamma_{\Omega}^{\uparrow}$ in the deep polar Southern Ocean for RCP8.5 are likely due to deep Southern Ocean waters preferentially upwelling at lower latitudes instead of being quickly mixed back to the Southern Ocean euphotic zone.

Changes in O_2^{pre} are driven by changes in euphotic O₂ and by changes in ventilation patterns. Figure B3 shows maps of the changes in euphotic-mean oxygen concentrations. Except at high latitudes, declines are widespread and attributable to warming-driven solubility reductions. Increases can be caused by decreased temperatures (e.g., in the North Atlantic cold blob) but the most intense increases occur near the Weddell and Ross Seas due to

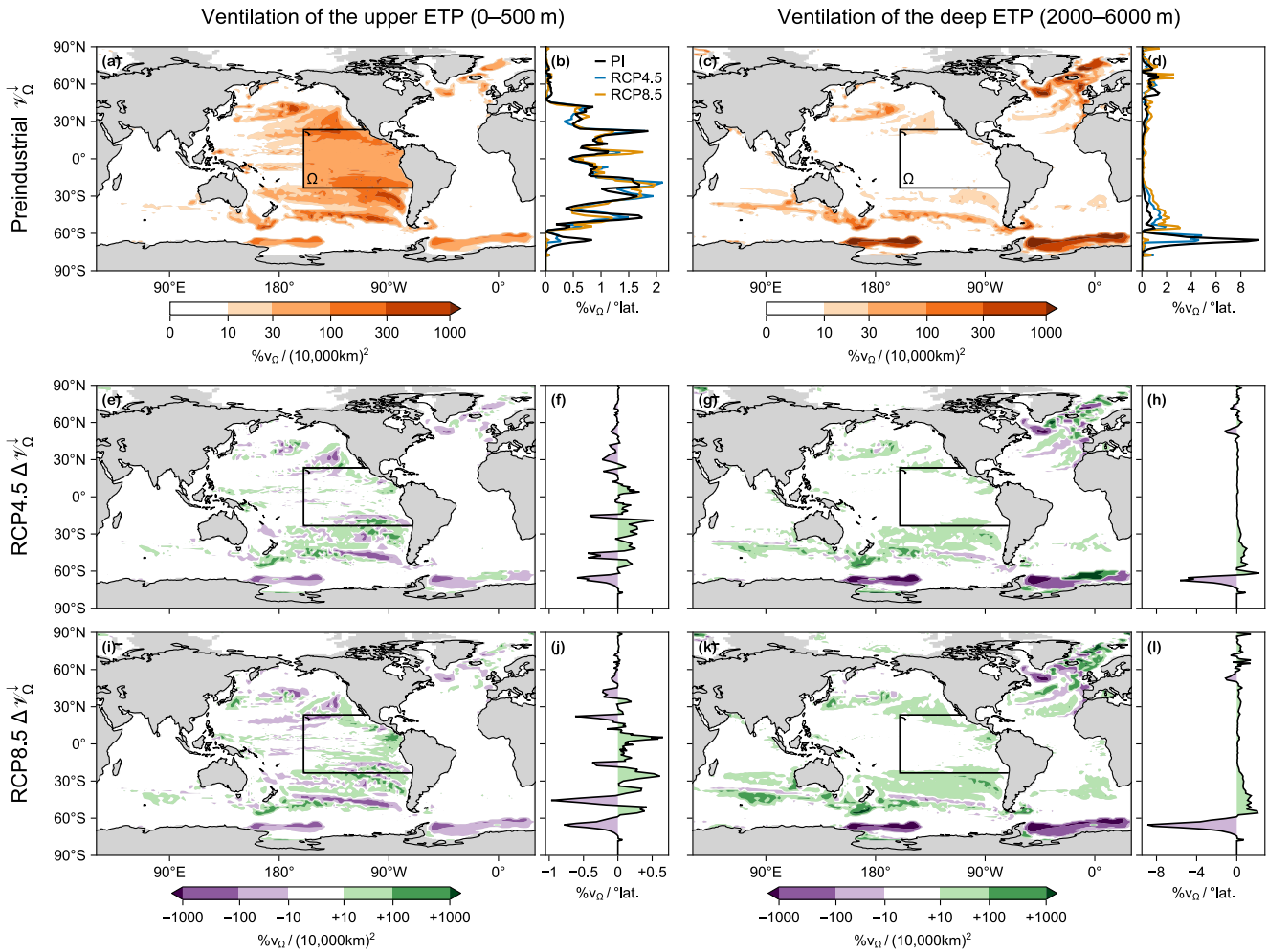


Figure B4. (a) Map and (b) zonal integral of the fractional Ω volume ventilated from the surface for Ω being the upper ETP (solid black contour), as quantified by $\mathcal{V}_{\Omega}^{\uparrow}$, in the preindustrial state. (c and d) As (a and b) for Ω being the deep ETP. (e–h) As (a–d) for $\Delta\mathcal{V}_{\Omega}^{\uparrow}$ in the RCP4.5 scenario. (i–l) As (e–h) in the RCP8.5 scenario. Note the nonlinear color scales.

reduced vertical mixing, which allows for better air–sea oxygen equilibration as discussed in Section 3.2 of the main text. However, solubility changes are not the dominant driver of reduced interior O_2^{pre} concentrations.

Decreases in the O_2^{pre} inventory of an interior subvolume Ω are dominantly driven by changes in ventilation patterns (Section 3.2), as quantified by the amount of the Ω volume ventilated per unit area, $\mathcal{V}_{\Omega}^{\uparrow}$. Maps of $\mathcal{V}_{\Omega}^{\uparrow}$ for Ω being the upper and deep ETP are plotted in Figure B4 for the preindustrial state, along with the changes for our perpetual-2090s states. The patterns of $\mathcal{V}_{\Omega}^{\uparrow}$ strongly mirror those of O_2^{pre} in Figure 9 of the main text. While $\sim 40\%$ of the upper ETP is ventilated from directly above, the remaining $\sim 60\%$ is ventilated from distant regions, with subtropical and subpolar contributions in the Pacific, as well as contributions from the North Atlantic, the Ross Sea, and the Weddell Sea. By contrast, the bulk of the deep ETP is ventilated from distant regions, with only about 1% from directly above. In our perpetual-2090s states, the subpolar and Southern Ocean contributions generally decline in favor of subtropical and tropical contributions, effectively shifting the origin of preformed O_2 equatorward where warmer waters hold less dissolved oxygen.

Data Availability Statement

The MATLAB and Julia code corresponding to this work is available at <https://zenodo.org/doi/10.5281/zenodo.13626655> (Pasquier, 2024). The figures were created in Julia (Bezanson et al., 2017) with the Makie.jl plotting

package (Danisch & Krumbiegel, 2021). The transport matrices were built from the historical, RCP4.5, and RCP8.5 ACCESS1.3 CMIP5 model runs available at <https://esgf.nci.org.au/projects/esgf-nci/>. This output also includes temperature, salinity, photosynthetically available radiation (PAR), mixed-layer depth (MLD), sea-ice, and wind fields.

Acknowledgments

This work was supported by Australian Research Council Grant DP210101650 (to MH) and undertaken with the assistance of resources and services from the National Computational Infrastructure (NCI), which is supported by the Australian Government. NLB support for this project received grant funding from the Australian Government as part of the Antarctic Science Collaboration Initiative program. Open access publishing facilitated by University of New South Wales, as part of the Wiley - University of New South Wales agreement via the Council of Australian University Librarians.

References

- Arias, P., Bellouin, N., Coppola, E., Jones, R., Krinner, G., Marotzke, J., et al. (2021). Technical summary [Book Section]. In V. Masson-Delmotte, G. M. Flato & N. Yassa (Eds.), *Climate change 2021: The physical science basis. Contribution of working group I to the sixth assessment report of the intergovernmental panel on climate change* (pp. 33–144). Cambridge University Press. <https://doi.org/10.1017/9781009157896.002>
- Bao, Y., & Li, Y. (2016). Simulations of dissolved oxygen concentration in CMIP5 Earth system models. *Acta Oceanologica Sinica*, 35(12), 28–37. <https://doi.org/10.1007/s13131-016-0959-x>
- Beman, J. M., & Carolan, M. T. (2013). Deoxygenation alters bacterial diversity and community composition in the ocean's largest oxygen minimum zone. *Nature Communications*, 4(1), 2705. <https://doi.org/10.1038/ncomms3705>
- Bezanson, J., Edelman, A., Karpinski, S., & Shah, V. B. (2017). Julia: A fresh approach to numerical computing. *SIAM Review*, 59(1), 65–98. <https://doi.org/10.1137/141000671>
- Bi, D., Marsland, S. J., Uotila, P., O'Farrell, S., Fiedler, R. A. S., Sullivan, A., et al. (2013). ACCESS-OM: The ocean and sea ice core of the ACCESS coupled model. *Australian Meteorological and Oceanographic Journal*, 63(1), 213–232. <https://doi.org/10.22499/2.6301.014>
- Bindoff, N. L., Cheung, W. W. L., Kairo, J. G., Aristegui, J., Guinder, V. A., Hallberg, R., et al. (2022). Changing ocean, marine ecosystems, and dependent communities. In *The ocean and cryosphere in a changing climate: Special report of the intergovernmental panel on climate change* (pp. 447–588). Cambridge University Press. <https://doi.org/10.1017/9781009157964.007>
- Bopp, L., Le Quéré, C., Heimann, M., Manning, A. C., & Monfray, P. (2002). Climate-induced oceanic oxygen fluxes: Implications for the contemporary carbon budget. *Global Biogeochemical Cycles*, 16(2), 6–16–13. <https://doi.org/10.1029/2001GB001445>
- Bopp, L., Resplandy, L., Orr, J. C., Doney, S. C., Dunne, J. P., Gehlen, M., et al. (2013). Multiple stressors of ocean ecosystems in the 21st century: Projections with CMIP5 models. *Biogeosciences*, 10(10), 6225–6245. <https://doi.org/10.5194/bg-10-6225-2013>
- Bopp, L., Resplandy, L., Untersee, A., Le Mezo, P., & Kageyama, M. (2017). Ocean (de)oxygenation from the Last Glacial Maximum to the twenty-first century: Insights from Earth system models. *Philosophical Transactions of the Royal Society A: Mathematical, Physical & Engineering Sciences*, 375(2102), 20160323. <https://doi.org/10.1098/rsta.2016.0323>
- Brandt, P., Bange, H. W., Banyte, D., Dengler, M., Didwischus, S.-H., Fischer, T., et al. (2015). On the role of circulation and mixing in the ventilation of oxygen minimum zones with a focus on the eastern tropical North Atlantic. *Biogeosciences*, 12(2), 489–512. <https://doi.org/10.5194/bg-12-489-2015>
- Breitburg, D., Levin, L. A., Oschlies, A., Grégoire, M., Chavez, F. P., Conley, D. J., et al. (2018). Declining oxygen in the global ocean and coastal waters. *Science*, 359(6371), eaam7240. <https://doi.org/10.1126/science.aam7240>
- Broecker, W. S., & Peng, T.-H. (1982). *Tracers in the sea* (Vol. 24, pp. b1–b2). Lamont-Doherty Geological Observatory, Columbia University Palisades. <https://doi.org/10.1017/S0033822200005221>
- Buchanan, P. J., & Tagliabue, A. (2021). The regional importance of oxygen demand and supply for historical ocean oxygen trends. *Geophysical Research Letters*, 48(20), e2021GL094797. <https://doi.org/10.1029/2021GL094797>
- Busecke, J. J. M., Resplandy, L., Ditkovsky, S. J., & John, J. G. (2022). Diverging fates of the Pacific Ocean oxygen minimum zone and its core in a warming world. *AGU Advances*, 3(6), e2021AV000470. <https://doi.org/10.1029/2021AV000470>
- Chamberlain, M. A., Matear, R. J., Holzer, M., Bi, D., & Marsland, S. J. (2019). Transport matrices from standard ocean-model output and quantifying circulation response to climate change. *Ocean Modelling*, 135, 1–13. <https://doi.org/10.1016/j.ocemod.2019.01.005>
- Chen, J.-J., Swart, N. C., Beadling, R., Cheng, X., Hattermann, T., Jüling, A., et al. (2023). Reduced deep convection and bottom water formation due to Antarctic meltwater in a multi-model ensemble. *Geophysical Research Letters*, 50(24), e2023GL106492. <https://doi.org/10.1029/2023GL106492>
- Cheng, L., von Schuckmann, K., Abraham, J. P., Trenberth, K. E., Mann, M. E., Zanna, L., et al. (2022). Past and future ocean warming. *Nature Reviews Earth & Environment*, 3(11), 776–794. <https://doi.org/10.1038/s43017-022-00345-1>
- Cliff, E., Khatiwala, S., & Schmittner, A. (2021). Glacial deep ocean deoxygenation driven by biologically mediated air–sea disequilibrium. *Nature Geoscience*, 14(1), 43–50. <https://doi.org/10.1038/s41561-020-00667-z>
- Couespel, D., Lévy, M., & Bopp, L. (2019). Major contribution of reduced upper ocean oxygen mixing to global ocean deoxygenation in an Earth system model. *Geophysical Research Letters*, 46(21), 12239–12249. <https://doi.org/10.1029/2019GL084162>
- Danisch, S., & Krumbiegel, J. (2021). Makie.jl: Flexible high-performance data visualization for Julia. *Journal of Open Source Software*, 6(65), 3349. <https://doi.org/10.21105/joss.03349>
- de Boyer Montégut, C., Madec, G., Fischer, A. S., Lazar, A., & Iudicone, D. (2004). Mixed layer depth over the global ocean: An examination of profile data and a profile-based climatology. *Journal of Geophysical Research*, 109(C12), C12003. <https://doi.org/10.1029/2004JC002378>
- de Lavergne, C., Palter, J. B., Galbraith, E. D., Bernardello, R., & Marinov, I. (2014). Cessation of deep convection in the open Southern Ocean under anthropogenic climate change. *Nature Climate Change*, 4(4), 278–282. <https://doi.org/10.1038/nclimate2132>
- Deutsch, C., Emerson, S., & Thompson, L. (2006). Physical-biological interactions in North Pacific oxygen variability. *Journal of Geophysical Research*, 111(C9), C09S90. <https://doi.org/10.1029/2005JC003179>
- Deutsch, C., Ferrel, A., Seibel, B., Pörtner, H.-O., & Huey, R. B. (2015). Climate change tightens a metabolic constraint on marine habitats. *Science*, 348(6239), 1132–1135. <https://doi.org/10.1126/science.aaa1605>
- Deutsch, C., Penn, J. L., & Lucey, N. (2024). Climate, oxygen, and the future of marine biodiversity. *Annual Review of Marine Science*, 16(1), 217–245. <https://doi.org/10.1146/annurev-marine-040323-095231>
- DeVries, T., & Deutsch, C. (2014). Large-scale variations in the stoichiometry of marine organic matter respiration. *Nature Geoscience*, 7(12), 890–894. <https://doi.org/10.1038/NGEO2300>
- Diaz, R. J., & Rosenberg, R. (2008). Spreading dead zones and consequences for marine ecosystems. *Science*, 321(5891), 926–929. <https://doi.org/10.1126/science.1156401>
- Doney, S. C., & Bullister, J. L. (1992). A chlorofluorocarbon section in the eastern North Atlantic. *Deep-Sea Research, Part A: Oceanographic Research Papers*, 39(11), 1857–1883. [https://doi.org/10.1016/0198-0149\(92\)90003-C](https://doi.org/10.1016/0198-0149(92)90003-C)

- Duteil, O., Koeve, W., Oschlies, A., Bianchi, D., Galbraith, E., Kriest, I., & Mear, R. (2013). A novel estimate of ocean oxygen utilisation points to a reduced rate of respiration in the ocean interior. *Biogeosciences*, *10*(11), 7723–7738. <https://doi.org/10.5194/bg-10-7723-2013>
- Earle, S. A., Wright, D. J., Joye, S., Laffoley, D., Baxter, J., Safina, C., & Elkus, P. (2018). Ocean deoxygenation: Time for action. *Science*, *359*(6383), 1475–1476. <https://doi.org/10.1126/science.aat0167>
- Eggleston, S., & Galbraith, E. D. (2018). The devil's in the disequilibrium: Multi-component analysis of dissolved carbon and oxygen changes under a broad range of forcings in a general circulation model. *Biogeosciences*, *15*(12), 3761–3777. <https://doi.org/10.5194/bg-15-3761-2018>
- Ekau, W., Auel, H., Pörtner, H.-O., & Gilbert, D. (2010). Impacts of hypoxia on the structure and processes in pelagic communities (zooplankton, macro-invertebrates and fish). *Biogeosciences*, *7*(5), 1669–1699. <https://doi.org/10.5194/bg-7-1669-2010>
- Espinoza-Morriberón, D., Echevin, V., Gutiérrez, D., Tam, J., Graco, M., Ledesma, J., & Colas, F. (2021). Evidences and drivers of ocean deoxygenation off Peru over recent past decades. *Scientific Reports*, *11*(1), 20292. <https://doi.org/10.1038/s41598-021-99876-8>
- Falkowski, P. G., & Godfrey, L. V. (2008). Electrons, life and the evolution of Earth's oxygen cycle. *Philosophical Transactions of the Royal Society B: Biological Sciences*, *363*(1504), 2705–2716. <https://doi.org/10.1098/rstb.2008.0054>
- Feely, R. A., Sabine, C. L., Schlitzer, R., Bullister, J. L., Mecking, S., & Greeley, D. (2004). Oxygen utilization and organic carbon remineralization in the upper water column of the Pacific Ocean. *Journal of Oceanography*, *60*(1), 45–52. <https://doi.org/10.1023/B:JOCE.0000038317.01279.aa>
- Franco, A. C., Kim, H., Frenzel, H., Deutsch, C., Ianson, D., Sumaila, U. R., & Tortell, P. D. (2022). Impact of warming and deoxygenation on the habitat distribution of Pacific halibut in the northeast Pacific. *Fisheries Oceanography*, *31*(6), 601–614. <https://doi.org/10.1111/fog.12610>
- Frölicher, T. L., Aschwanden, M. T., Gruber, N., Jaccard, S. L., Dunne, J. P., & Paynter, D. (2020). Contrasting upper and deep ocean oxygen response to protracted global warming. *Global Biogeochemical Cycles*, *34*(8), e2020GB006601. <https://doi.org/10.1029/2020GB006601>
- Fu, W., Bardin, A., & Primeau, F. W. (2018). Tracing ventilation source of tropical Pacific oxygen minimum zones with an adjoint global ocean transport model. *Deep Sea Research Part I: Oceanographic Research Papers*, *139*, 95–103. <https://doi.org/10.1016/j.dsr.2018.07.017>
- Gallo, N. D., & Levin, L. A. (2016). Chapter three—Fish ecology and evolution in the world's oxygen minimum zones and implications of ocean deoxygenation. In B. E. Curry (Ed.), *Advances in marine biology* (Vol. 74, pp. 117–198). Academic Press. <https://doi.org/10.1016/bs.amb.2016.04.001>
- Gnanadesikan, A., Dunne, J. P., & John, J. (2012). Understanding why the volume of suboxic waters does not increase over centuries of global warming in an Earth System Model. *Biogeosciences*, *9*(3), 1159–1172. <https://doi.org/10.5194/bg-9-1159-2012>
- Graco, M. I., Purca, S., Dewitte, B., Castro, C. G., Morón, O., Ledesma, J., et al. (2017). The OMZ and nutrient features as a signature of interannual and low-frequency variability in the Peruvian upwelling system. *Biogeosciences*, *14*(20), 4601–4617. <https://doi.org/10.5194/bg-14-4601-2017>
- Gunn, K. L., Rintoul, S. R., England, M. H., & Bowen, M. M. (2023). Recent reduced abyssal overturning and ventilation in the Australian Antarctic Basin. *Nature Climate Change*, *13*(6), 537–544. <https://doi.org/10.1038/s41558-023-01667-8>
- Helm, K. P., Bindoff, N. L., & Church, J. A. (2011). Observed decreases in oxygen content of the global ocean. *Geophysical Research Letters*, *38*(23), L23602. <https://doi.org/10.1029/2011GL049513>
- Heuzé, C., Heywood, K. J., Stevens, D. P., & Ridley, J. K. (2013). Southern Ocean bottom water characteristics in CMIP5 models. *Geophysical Research Letters*, *40*(7), 1409–1414. <https://doi.org/10.1002/grl.50287>
- Heuzé, C., Heywood, K. J., Stevens, D. P., & Ridley, J. K. (2015). Changes in global ocean bottom properties and volume transports in CMIP5 models under climate change scenarios. *Journal of Climate*, *28*(8), 2917–2944. <https://doi.org/10.1175/JCLI-D-14-00381.1>
- Hofmann, A. F., Peltzer, E. T., Walz, P. M., & Brewer, P. G. (2011). Hypoxia by degrees: Establishing definitions for a changing ocean. *Deep Sea Research Part I: Oceanographic Research Papers*, *58*(12), 1212–1226. <https://doi.org/10.1016/j.dsr.2011.09.004>
- Holzer, M. (2022). The fate of oxygen in the ocean and its sensitivity to local changes in biological production. *Journal of Geophysical Research: Oceans*, *127*(8), e2022JC018802. <https://doi.org/10.1029/2022JC018802>
- Holzer, M., Chamberlain, M. A., & Mear, R. J. (2020). Climate-driven changes in the ocean's ventilation pathways and time scales diagnosed from transport matrices. *Journal of Geophysical Research: Oceans*, *125*(10), e2020JC016414. <https://doi.org/10.1029/2020JC016414>
- Holzer, M., DeVries, T., & de Lavergne, C. (2021). Diffusion controls the ventilation of a Pacific Shadow Zone above abyssal overturning. *Nature Communications*, *12*(1), 4348. <https://doi.org/10.1038/s41467-021-24648-x>
- Holzer, M., & Hall, T. M. (2000). Transit-time and tracer-age distributions in geophysical flows. *Journal of the Atmospheric Sciences*, *57*(21), 3539–3558. [https://doi.org/10.1175/1520-0469\(2000\)057<3539:TTATAD>2.0.CO;2](https://doi.org/10.1175/1520-0469(2000)057<3539:TTATAD>2.0.CO;2)
- Ito, T. (2022). Optimal interpolation of global dissolved oxygen: 1965–2015. *Geoscience Data Journal*, *9*(1), 167–176. <https://doi.org/10.1002/gdj3.130>
- Ito, T., Follows, M. J., & Boyle, E. A. (2004). Is AOU a good measure of respiration in the oceans? *Geophysical Research Letters*, *31*(17), L17305. <https://doi.org/10.1029/2004GL020900>
- Ito, T., Garcia, H. E., Wang, Z., Minobe, S., Long, M. C., Cebrían, J., et al. (2024). Underestimation of multi-decadal global O₂ loss due to an optimal interpolation method. *Biogeosciences*, *21*(3), 747–759. <https://doi.org/10.5194/bg-21-747-2024>
- Ito, T., Minobe, S., Long, M. C., & Deutsch, C. (2017). Upper ocean O₂ trends: 1958–2015. *Geophysical Research Letters*, *44*(9), 4214–4223. <https://doi.org/10.1002/2017GL073613>
- Ito, T., Takano, Y., Deutsch, C., & Long, M. C. (2022). Sensitivity of global ocean deoxygenation to vertical and isopycnal mixing in an ocean biogeochemistry model. *Global Biogeochemical Cycles*, *36*(4), e2021GB007151. <https://doi.org/10.1029/2021GB007151>
- Jin, X., Najjar, R. G., Louanchi, F., & Doney, S. C. (2007). A modeling study of the seasonal oxygen budget of the global ocean. *Journal of Geophysical Research*, *112*(C5), C05017. <https://doi.org/10.1029/2006JC003731>
- Keeling, R. F., & Garcia, H. E. (2002). The change in oceanic O₂ inventory associated with recent global warming. *Proceedings of the National Academy of Sciences of the United States of America*, *99*(12), 7848–7853. <https://doi.org/10.1073/pnas.122154899>
- Keeling, R. F., Körtzinger, A., & Gruber, N. (2010). Ocean deoxygenation in a warming world. *Annual Review of Marine Science*, *2*(1), 199–229. <https://doi.org/10.1146/annurev.marine.010908.163855>
- Koeve, W., & Kähler, P. (2016). Oxygen utilization rate (OUR) underestimates ocean respiration: A model study. *Global Biogeochemical Cycles*, *30*(8), 1166–1182. <https://doi.org/10.1029/2015GB005354>
- Kwiatkowski, L., Torres, O., Bopp, L., Aumont, O., Chamberlain, M., Christian, J. R., et al. (2020). Twenty-first century ocean warming, acidification, deoxygenation, and upper-ocean nutrient and primary production decline from CMIP6 model projections. *Biogeosciences*, *17*(13), 3439–3470. <https://doi.org/10.5194/bg-17-3439-2020>
- Laffoley, D., & Baxter, J. M. (2019). *Ocean deoxygenation: Everyone's problem: Causes, impacts, consequences and solutions: Summary for policy makers (Report)*. Gland: International Union for Conservation of Nature (IUCN). <https://doi.org/10.2305/IUCN.CH.2019.14.en>
- Lauvset, S. K., Key, R. M., Olsen, A., van Heuven, S., Velo, A., Lin, X., et al. (2016). A new global interior ocean mapped climatology: The 1 × 1 GLODAP version 2. *Earth System Science Data*, *8*(2), 325–340. <https://doi.org/10.5194/essd-8-325-2016>

- Levin, L. A. (2018). Manifestation, drivers, and emergence of open ocean deoxygenation. *Annual Review of Marine Science*, 10(1), 229–260. <https://doi.org/10.1146/annurev-marine-121916-063359>
- Li, Q., England, M. H., Hogg, A. M., Rintoul, S. R., & Morrison, A. K. (2023). Abyssal ocean overturning slowdown and warming driven by Antarctic meltwater. *Nature*, 615(7954), 841–847. <https://doi.org/10.1038/s41586-023-05762-w>
- Long, M. C., Ito, T., & Deutsch, C. (2019). Oxygen projections for the future. In *Ocean deoxygenation: Everyone's problem—Causes, impacts, consequences and solutions* (pp. 171–211). IUCN.
- Marsland, S., Bi, D., Uotila, P., Fiedler, R., Griffies, S., Lorbacher, K., et al. (2013). Configuration and spin-up of ACCESS-CM2, the new generation Australian Community Climate and Earth System Simulator Coupled Model. *Australian Meteorological and Oceanographic Journal*, 63(1), 101–119. <https://doi.org/10.22499/2.6301.007>
- Matear, R. J., & Hirst, A. C. (2003). Long-term changes in dissolved oxygen concentrations in the ocean caused by protracted global warming. *Global Biogeochemical Cycles*, 17(4). <https://doi.org/10.1029/2002GB001997>
- Matear, R. J., Hirst, A. C., & McNeil, B. I. (2000). Changes in dissolved oxygen in the Southern Ocean with climate change. *Geochemistry, Geophysics, Geosystems*, 1(11), 1050. <https://doi.org/10.1029/2000GC000086>
- McCormick, L. R., & Levin, L. A. (2017). Physiological and ecological implications of ocean deoxygenation for vision in marine organisms. *Philosophical Transactions of the Royal Society A: Mathematical, Physical & Engineering Sciences*, 375(2102), 20160322. <https://doi.org/10.1098/rsta.2016.0322>
- Meinshausen, M., Nicholls, Z. R. J., Lewis, J., Gidden, M. J., Vogel, E., Freund, M., et al. (2020). The shared socio-economic pathway (SSP) greenhouse gas concentrations and their extensions to 2500. *Geoscientific Model Development*, 13(8), 3571–3605. <https://doi.org/10.5194/gmd-13-3571-2020>
- Meinshausen, M., Smith, S. J., Calvin, K., Daniel, J. S., Kainuma, M. L. T., Lamarque, J.-F., et al. (2011). The RCP greenhouse gas concentrations and their extensions from 1765 to 2300. *Climatic Change*, 109(1), 213–241. <https://doi.org/10.1007/s10584-011-0156-z>
- Mongwe, P., Long, M., Ito, T., Deutsch, C., & Santana-Falcón, Y. (2024). Climatic controls on metabolic constraints in the ocean. *Biogeosciences*, 21(15), 3477–3490. <https://doi.org/10.5194/bg-21-3477-2024>
- Moore, J. K., Fu, W., Primeau, F. W., Britten, G. L., Lindsay, K., Long, M., et al. (2018). Sustained climate warming drives declining marine biological productivity. *Science*, 359(6380), 1139–1143. <https://doi.org/10.1126/science.aao6379>
- Morée, A. L., Clarke, T. M., Cheung, W. W. L., & Frölicher, T. L. (2023). Impact of deoxygenation and warming on global marine species in the 21st century. *Biogeosciences*, 20(12), 2425–2454. <https://doi.org/10.5194/bg-20-2425-2023>
- Oschlies, A. (2021). A committed fourfold increase in ocean oxygen loss. *Nature Communications*, 12(1), 2307. <https://doi.org/10.1038/s41467-021-22584-4>
- Oschlies, A., Brandt, P., Stramma, L., & Schmidtko, S. (2018). Drivers and mechanisms of ocean deoxygenation. *Nature Geoscience*, 11(7), 467–473. <https://doi.org/10.1038/s41561-018-0152-2>
- Oschlies, A., Koeve, W., Landolfi, A., & Kähler, P. (2019). Loss of fixed nitrogen causes net oxygen gain in a warmer future ocean. *Nature Communications*, 10(1), 2805. <https://doi.org/10.1038/s41467-019-10813-w>
- Palter, J. B., & Trossman, D. S. (2018). The sensitivity of future ocean oxygen to changes in ocean circulation. *Global Biogeochemical Cycles*, 32(5), 738–751. <https://doi.org/10.1002/2017GB005777>
- Pascal, L., Cool, J., Archambault, P., Calosi, P., Cuenca, A. L. R., Mucci, A. O., & Chaillou, G. (2023). Ocean deoxygenation caused non-linear responses in the structure and functioning of benthic ecosystems. *Global Change Biology*, 30(1), e16994. <https://doi.org/10.1111/gcb.16994>
- Pasquier, B. (2024). Code for Deoxygenation and Its Drivers Analyzed in Steady State for Perpetually Slower and Warmer Oceans. *Zenodo*. <https://doi.org/10.5281/zenodo.13626656>
- Pasquier, B., Holzer, M., & Chamberlain, M. A. (2024). The biological and preformed carbon pumps in perpetually slower and warmer oceans. *Biogeosciences*, 21(14), 3373–3400. <https://doi.org/10.5194/bg-21-3373-2024>
- Pasquier, B., Holzer, M., Chamberlain, M. A., Matear, R. J., Bindoff, N. L., & Primeau, F. W. (2023). Optimal parameters for the ocean's nutrient, carbon, and oxygen cycles compensate for circulation biases but re-plumb the biological pump. *Biogeosciences*, 20(14), 2985–3009. <https://doi.org/10.5194/bg-20-2985-2023>
- Pitcher, G. C., Aguirre-Velarde, A., Breitburg, D., Cardich, J., Carstensen, J., Conley, D. J., et al. (2021). System controls of coastal and open ocean oxygen depletion. *Progress in Oceanography*, 197, 102613. <https://doi.org/10.1016/j.poccean.2021.102613>
- Plattner, G.-K., Joos, F., Stocker, T. F., & Marchal, O. (2001). Feedback mechanisms and sensitivities of ocean carbon uptake under global warming. *Tellus B: Chemical and Physical Meteorology*, 53(5), 564–592. <https://doi.org/10.3402/tellusb.v53i5.16637>
- Primeau, F. W. (2005). Characterizing transport between the surface mixed layer and the ocean interior with a forward and adjoint global ocean transport model. *Journal of Physical Oceanography*, 35(4), 545–564. <https://doi.org/10.1175/JPO2699.1>
- Purich, A., & England, M. H. (2023). Projected impacts of Antarctic meltwater anomalies over the twenty-first century. *Journal of Climate*, 36(8), 2703–2719. <https://doi.org/10.1175/JCLI-D-22-0457.1>
- Purich, A., England, M. H., Cai, W., Sullivan, A., & Durack, P. J. (2018). Impacts of broad-scale surface freshening of the Southern Ocean in a coupled climate model. *Journal of Climate*, 31(7), 2613–2632. <https://doi.org/10.1175/JCLI-D-17-0092.1>
- Riahi, K., van Vuuren, D. P., Kriegler, E., Edmonds, J., O'Neill, B. C., Fujimori, S., et al. (2017). The shared socioeconomic pathways and their energy, land use, and greenhouse gas emissions implications: An overview. *Global Environmental Change*, 42, 153–168. <https://doi.org/10.1016/j.gloenvcha.2016.05.009>
- Roach, C. J., & Bindoff, N. L. (2023). Developing a new oxygen atlas of the world's oceans using data interpolating variational analysis. *Journal of Atmospheric and Oceanic Technology*, 40(11), 1475–1491. <https://doi.org/10.1175/JTECH-D-23-0007.1>
- Rogers, A. D. (2000). The role of the oceanic oxygen minima in generating biodiversity in the deep sea. *Deep Sea Research Part II: Topical Studies in Oceanography*, 47(1), 119–148. [https://doi.org/10.1016/S0967-0645\(99\)00107-1](https://doi.org/10.1016/S0967-0645(99)00107-1)
- Russell, J. L., & Dickson, A. G. (2003). Variability in oxygen and nutrients in South Pacific Antarctic Intermediate Water. *Global Biogeochemical Cycles*, 17(2). <https://doi.org/10.1029/2000GB001317>
- Sarmiento, J. L., Herbert, T. D., & Toggweiler, J. R. (1988). Causes of anoxia in the world ocean. *Global Biogeochemical Cycles*, 2(2), 115–128. <https://doi.org/10.1029/GB002i002p00115>
- Sato, K. N., Levin, L. A., & Schiff, K. (2017). Habitat compression and expansion of sea urchins in response to changing climate conditions on the California continental shelf and slope (1994–2013). *Deep Sea Research Part II: Topical Studies in Oceanography*, 137, 377–389. <https://doi.org/10.1016/j.dsr2.2016.08.012>
- Schmidtko, S., Stramma, L., & Visbeck, M. (2017). Decline in global oceanic oxygen content during the past five decades. *Nature*, 542(7641), 335–339. <https://doi.org/10.1038/nature21399>

- Schmittner, A., Oschlies, A., Matthews, H. D., & Galbraith, E. D. (2008). Future changes in climate, ocean circulation, ecosystems, and biogeochemical cycling simulated for a business-as-usual CO₂ emission scenario until year 4000 AD. *Global Biogeochemical Cycles*, 22(1). <https://doi.org/10.1029/2007GB002953>
- Seibel, B. A. (2011). Critical oxygen levels and metabolic suppression in oceanic oxygen minimum zones. *Journal of Experimental Biology*, 214(2), 326–336. <https://doi.org/10.1242/jeb.049171>
- Shaffer, G., Olsen, S. M., & Pedersen, J. O. P. (2009). Long-term ocean oxygen depletion in response to carbon dioxide emissions from fossil fuels. *Nature Geoscience*, 2(2), 105–109. <https://doi.org/10.1038/ngeo420>
- Sonnerup, R. E., Mecking, S., & Bullister, J. L. (2013). Transit time distributions and oxygen utilization rates in the northeast Pacific Ocean from chlorofluorocarbons and sulfur hexafluoride. *Deep Sea Research Part I: Oceanographic Research Papers*, 72, 61–71. <https://doi.org/10.1016/j.dsr.2012.10.013>
- Sonnerup, R. E., Mecking, S., Bullister, J. L., & Warner, M. J. (2015). Transit time distributions and oxygen utilization rates from chlorofluorocarbons and sulfur hexafluoride in the southeast Pacific Ocean. *Journal of Geophysical Research: Oceans*, 120(5), 3761–3776. <https://doi.org/10.1002/2015JC010781>
- Srokosz, M. A., & Bryden, H. L. (2015). Observing the Atlantic Meridional Overturning Circulation yields a decade of inevitable surprises. *Science*, 348(6241), 1255–1257. <https://doi.org/10.1126/science.1255575>
- Stramma, L., Prince, E. D., Schmidtko, S., Luo, J., Hoolihan, J. P., Visbeck, M., et al. (2012). Expansion of oxygen minimum zones may reduce available habitat for tropical pelagic fishes. *Nature Climate Change*, 2(1), 33–37. <https://doi.org/10.1038/nclimate1304>
- Takano, Y., Ilyina, T., Tjiputra, J., Eddebban, Y. A., Berthet, S., Bopp, L., et al. (2023). Simulations of ocean deoxygenation in the historical era: Insights from forced and coupled models. *Frontiers in Marine Science*, 10. <https://doi.org/10.3389/fmars.2023.1139917>
- Thomas, J. L., Waugh, D. W., & Gnanadesikan, A. (2020). Relationship between age and oxygen along line W in the northwest Atlantic Ocean. *Ocean Science Journal*, 55(2), 203–217. <https://doi.org/10.1007/s12601-020-0019-5>
- Vaquier-Sunyer, R., & Duarte, C. M. (2008). Thresholds of hypoxia for marine biodiversity. *Proceedings of the National Academy of Sciences of the United States of America*, 105(40), 15452–15457. <https://doi.org/10.1073/pnas.0803833105>
- Wanninkhof, R. (2014). Relationship between wind speed and gas exchange over the ocean revisited. *Limnology and Oceanography: Methods*, 12(6), 351–362. <https://doi.org/10.4319/lom.2014.12.351>
- Warner, M. J., Bullister, J. L., Wisegarver, D. P., Gammon, R. H., & Weiss, R. F. (1996). Basin-wide distributions of chlorofluorocarbons CFC-11 and CFC-12 in the North Pacific: 1985–1989. *Journal of Geophysical Research*, 101(C9), 20525–20542. <https://doi.org/10.1029/96JC01849>
- Whitney, F. A., Freeland, H. J., & Robert, M. (2007). Persistently declining oxygen levels in the interior waters of the eastern subarctic Pacific. *Progress in Oceanography*, 75(2), 179–199. <https://doi.org/10.1016/j.pocean.2007.08.007>
- Wishner, K. F., Seibel, B. A., Roman, C., Deutsch, C., Outram, D., Shaw, C. T., et al. (2018). Ocean deoxygenation and zooplankton: Very small oxygen differences matter. *Science Advances*, 4(12), eaau5180. <https://doi.org/10.1126/sciadv.aau5180>
- Wyrski, K. (1962). The oxygen minima in relation to ocean circulation. *Deep-Sea Research and Oceanographic Abstracts*, 9(1), 11–23. [https://doi.org/10.1016/0011-7471\(62\)90243-7](https://doi.org/10.1016/0011-7471(62)90243-7)
- Zheng, Y., Schlosser, P., Swift, J. H., & Jones, E. P. (1997). Oxygen utilization rates in the Nansen Basin, Arctic Ocean: Implications for new production. *Deep Sea Research Part I: Oceanographic Research Papers*, 44(12), 1923–1943. [https://doi.org/10.1016/S0967-0637\(97\)00046-0](https://doi.org/10.1016/S0967-0637(97)00046-0)